Taylor & Francis
Taylor & Francis Group

Corrosion Engineering, Science and Technology
The International Journal of Corrosion Processes and Corrosion Control

ISSN: (Print) (Online) Journal homepage: https://www.tandfonline.com/loi/ycst20

TSA anodising voltage effects on the near-surface coarse intermetallic particles in the AA2024-T3 and AA2198-T8 alloys

João Victor de Sousa Araujo, Mariana Xavier Milagre, Rafael Emil Klumpp, Victor Hugo Ayusso, Uyime Donatus & Isolda Costa

To cite this article: João Victor de Sousa Araujo, Mariana Xavier Milagre, Rafael Emil Klumpp, Victor Hugo Ayusso, Uyime Donatus & Isolda Costa (2022) TSA anodising voltage effects on the near-surface coarse intermetallic particles in the AA2024-T3 and AA2198-T8 alloys, Corrosion Engineering, Science and Technology, 57:4, 380-396, DOI: 10.1080/1478422X.2022.2071666

To link to this article: https://doi.org/10.1080/1478422X.2022.2071666

CORROSION ENGINEERING, SCIENCE AND TECHNOLOGY
2022, VOL. 57, NO. 4, 380–396
https://doi.org/10.1080/1478422X.2022.2071666

Institute of Materials, Minerals & Mining
Taylor & Francis
Taylor & Francis Group

RESEARCH ARTICLE

TSA anodising voltage effects on the near-surface coarse intermetallic particles in the AA2024-T3 and AA2198-T8 alloys

João Victor de Sousa Araujo, Mariana Xavier Milagre, Rafael Emil Klumpp, Victor Hugo Ayusso, Uyime Donatus and Isolda Costa

Materials Science and Technology Center, Nuclear and Energy Research Institute – IPEN/CNEN – Av. Prof. Lineu Prestes, São Paulo, Brazil

ABSTRACT
In this study, the behaviour of the micrometric particles of the AA2198-T8 alloy during anodising at various voltages and the effect of anodising voltage on the anodised surface morphology have been investigated in a tartaric-sulfuric acid anodising solution. The results were compared with that of the AA2024-T3 alloy. For the AA2198-T8 alloy, partial dissolution of these particles occurred at 0, 3 and 4 V. Besides, for potentials above 5 V, there is a preferential dissolution of the intermetallic particles. For the AA2024-T3 alloy, the results indicated a total dissolution of the micrometric particles at 0 V and a partial dissolution at 3 V, whereas above 4 V total dissolution occurred. Between 1 and 2 V, no dissolution was observed for both alloys. The preferential dissolution of the micrometric particles resulted in defects in the anodic film and cavities on the anodised surfaces.

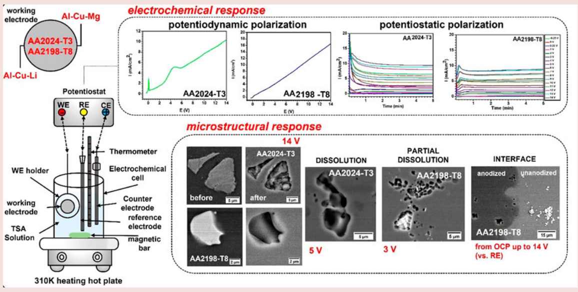

ARTICLE HISTORY
Received 13 February 2022
Accepted 25 April 2022

KEYWORDS
Al alloys; anodising; TSA; intermetallic particles

Introduction

Aluminium alloys of the 2XXX series are important for aerospace applications due to their high specific strengths [1,2]. The new generation of Cu-containing Al alloys, such as the Al-Cu-Li ones, are being produced for the improvement of specific strength requirements [3–6]. These alloys have been considered as potential substitutes for conventional Al-Cu-Mg alloys, such as AA2024. According to Chen et al. [7], the C919 aircraft developed by Chinese state-owned COMAC has 15.5% of its structures made of Al-Cu-Li alloys allowing 7% of the structure weight reduction. They also stand out in that the annual demand for Al-Cu-Li alloys in China over the next decade is estimated to be more than 1500 t and that these alloys will gradually become the primary choice for the new generation of commercial aircraft structures [8–10]. However, these alloys have heterogeneous microstructures due to the intermetallic particles that are formed during solidification and thermomechanical treatment processes [11]. This heterogeneity has been related to the high susceptibility of these alloys to localised corrosion as a result of galvanic cells forming between different phases and the matrix [6,12–17].

In the last years, many works were carried out in order to understand the corrosion mechanism and the corrosion resistance of the AA2024 alloy [18–28,12] and also of the Al-Cu-Li alloys [4,11,29–37]. Recently, some researchers reported the effect of microstructure on the corrosion initiation in Al-Cu and Al-Cu-Li alloys [38–54]. All these works demonstrated the higher susceptibility of these alloys to localised corrosion and the need for corrosion protection.

An efficient method used industrially to avoid localised corrosion is chromic acid anodising. This process consists in favouring oxide layer growth on the aluminium substrate in a chromic acid solution through the application of electric potentials. However, this method is not environmentally friendly due to the highly toxic chromium VI ions residues generated, which remains partially in the oxide layer after the anodising process [55–58]. Thus, anodising methods in mixed electrolytes, such as the tartaric-sulfuric acid anodising are currently being considered as substitutes for chromic acid anodising [59–61].

Besides the effect on corrosion propagation, the presence of coarse intermetallic particles significantly affects the anodising response of aluminium alloys. Additionally, the behaviour of particles during anodising is far from being fully understood. Over the years, some research works have been carried out on this subject. For example, Zahavi et al. [62], Iglesias-Rubianes et al. [63], Curione et al. [64],

CONTACT João Victor de Sousa Araujo joao-neutron@hotmail.com Materials Science and Technology Center, Nuclear and Energy Research Institute – IPEN/CNEN – Av. Prof. Lineu Prestes, 2242 São Paulo, SP, Brazil

Supplemental data for this article can be accessed online at https://doi.org/10.1080/1478422X.2022.2071666.

Table 1. The behaviour of the coarse IMPs presents in alloys from the 2XXX series during the anodising process.

Alloy	Phase	Electrolyte	Behaviour during the anodisation	Ref.
Al-Cu alloys				
AA2024	Al-Cu-Mg	Sulfuric acid	Partial dissolution, partial oxidation.	[62]
	Cu behaviour	Ammonium pentaborate	The generation of gaseous oxygen was associated with the incorporation of Cu species into the anodic film	[63]
	Al-Cu-Mg	Sulfuric acid	Selective dissolution during anodising	[64]
	Al_2MgCu Al_2Cu		The phases started to oxidise at 0, 1.8 and 2 V SCE, respectively.	[65]
	Al-Cu-Mg Al-Cu-Fe-Mn-Si Al_2Cu		The phases containing Mg were easily oxidised compared to the second phases containing only Al, and Cu and/or Fe	[66]
	S′- Al_2CuMg		Particles oxidised preferentially above 0 V	[67]
AA2017	Al_2Cu Al_2CuMg		Al_2CuMg particles exhibited anodic electrochemical behaviour concerning the matrix; Al_2Cu, exhibited a cathodic electrochemical behaviour	[68, 69]
AA2011	Al-Cu-Fe Al-Cu-Bi Al-Cu-Bi-Pb-Fe		Al-Cu-Fe particles were dissolved in the electrolyte creating voids in the layer; Al-Cu-Bi and Al-Cu-Bi-Pb-Fe were occluded in the anodic film	[70]
AA2014	Al_2CuMg		The dissolution of intermetallics during anodising induced the formation of cavities in the anodic layer	[71]
	Al_2Cu			[73]
AA2618	Al_2CuMg		The anodised layer contains defects related to the size and composition of the intermetallic phases	[72]
Al-Cu-Li alloys				
AA2050	Al-Cu-Fe-Mn	Sulfuric acid	Partial dissolution and embedment	[74]
AA2099	Al-Fe-Mn-Cu with variable Cu levels (low-, medium- and high-copper content) Al_3Zn Al-Fe-Mn-Li	Tartaric-Sulfuric Acid	Al-Fe-Mn-Cu particles with low-copper content were anodised at approximately the same oxidation rate as the alloy matrix,; Al-Fe-Mn-Cu particles with medium-copper content were found in the electrolyte due to their poor adhesion to the substrate and high solubility in the acid environment; Al-Fe-Mn-Cu particles with a high Cu content were rapidly dissolved during anodising, resulting in cavities in the anodic film; Al-Fe-Mn-Li particles were anodised at a slightly lower rate than the alloy matrix, forming a less regular porous anodic film compared to the matrix; the Al_3Zn dispersoids were anodised at a rate similar to that of the alloy matrix	[75]
	Al_2Cu		Cu present in the particles could be occluded in the anodic film as Cu-rich nanoparticles or oxidised and incorporated into the film material as Cu ions	[76]
	Al-Fe-Mn-Cu		Partial dissolution, partial oxidation.	[77]
	Li-rich particles	Sulfuric acid	Particles became occluded in the anodic film and were partially dissolved in the electrolyte	[79]
	Al-Fe-Mn-Cu	Tartaric-Sulfuric Acid	Particles with high Cu content (HCCPs) dissolved in the electrolyte preferentially at 0 V	[80]
	T1 (Al_2CuLi)		The precipitates were anodised faster than the Al matrix in the solution under a constant voltage of 14 V	[78]
AA2297	Al-Fe-Mn-Cu	Adipic-Sulfuric Acid	The particles containing high Cu content (HCCPs) were preferably dissolved around 0.1 and dissolved completely at the 3 V, the particles containing medium Cu content (LCCPs) were not dissolved at 0.1 V but were oxidised at 3 V; the nanoparticles containing Cu-Mn-Fe remained on the surface at potentials below 3 V and, they were dissolved above 3 V	[81]
AA2055	Al-Fe-Mn-Cu	Tartaric-Sulfuric Acid	The anodisation of the intermetallics resulted in the formation of micrometric sized cavities on the anodic film	[82]
	Al-Cu-Fe	H_2SO_4	It was observed some imperfections (cavity) on the surface due to the local dissolution of the particles	[83]

Saenz de Miera et al. [65,66] and Nickel et al. [67] studied the effect of micrometric particles on the anodising behaviour of the AA2024 alloy. Also, Fares et al. [68,69], Bononi et al. [70], Abdel-Gawad et al. [71], Veys-Renaux et al. [72] and Elkilany et al. [73] carried out works on the effect of micrometric particles on the anodising of other alloys different from the Al-Cu-Mg series. For the Al-Cu-Li alloys, the works of Viejo et al. [74], Ma et al. [75–78], Bononi et al. [79] and Wu et al. [80] explain the behaviour of the AA2099 alloy during anodising. Moreover, Liu et al. [81] reported on the behaviour of the AA2297 alloy; and Ma et al. [82] and Samaniego-Gámez et al. [83] described the effect of micrometric particles on the AA2055 alloy anodising. Table 1 shows the intermetallic particles (IMPs) studied in these works and their b during anodising.

Reports on the Al-Cu-Mg AA2024 alloy are numerous, whereas studies on Al-Cu-Li alloys are mainly related to the AA2099, but the behaviour of other Al-Cu-Li commercial alloys with different Li, Mn and Ag contents, can also be found [74,81–83]. The first Al-Cu-Li alloys applied in commercial aircrafts were provided by ALCOA [84]. Currently, other companies are manufacturing different grades of Al-Cu-Li alloys. For example, Commercial Aircraft Corporation of China Ltd. (COMAC), and the Southwest Aluminium Corporation (Beijing, China), known as CHINALCO, are producing the AA2195, AA2197, AA2A97, AA2099, AA2198 alloys [9,81,82,85–87]. Besides the Chinese companies, the AA2198 alloy is also produced by Kenlian Aluminium, in the United States, and by the European company, Constellium [9].

The AA2198 alloy has been the object of numerous corrosion studies [4,11,30,42,43,88–93]. However, the behaviour of the coarse intermetallic particles during anodising has not yet been reported. This work intends to fill this gap in the literature. For this purpose, the morphology, chemical composition and surface distribution of the intermetallic particles were evaluated by scanning electron microscopy (SEM), energy-dispersive X-ray spectroscopy (EDX) and atomic force microscopy (AFM) techniques. Additionally, the role of the coarse intermetallic particles during TSA anodising process was investigated by potentiodynamic polarisation and potentiostatic polarisation tests under conditions which simulates those industrially performed. SEM images were obtained, before and after anodising, in order to identify the influence of this process on the material surface.

Table 2. Chemical composition of the studied alloys (wt-%) obtained by inductively coupled plasma optical emission spectrometry (ICP-OES).

	Aluminium alloys	
Elements	AA2024-T3	AA2198-T8
Al	Balance	Balance
Cu	4.8	3.34
Mg	0.59	0.31
Mn	0.52	0.003
Li	–	0.95
Fe	0.18	0.04
Zn	0.11	0.006
Si	0.07	0.04
Zr	–	0.50
Ag	–	0.26

Taking into consideration that many works reported the importance of comparing the mechanical [94–97] and corrosion [24,43,98–100] properties of the AA2024 alloys with that of the Al-Cu-Li alloys, the behaviour of the coarse particles in the AA2024-T3 Al-Cu-Mg alloy during anodising was also evaluated and reported. The results presented are helpful for the development of novel surface treatments for the optimal performance of these aluminium alloys in service.

Materials and methods

Disc-shaped samples of the AA2024-T3 and AA2198-T8 alloys with a diameter of 1.5 cm were used in this study. The chemical composition of both alloys is shown in Table 2. The samples were mechanically and sequentially ground with silicon carbide papers (#400, #800, #1400 and #4000) and subsequently polished with diamond pastes of 3 and 1 µm. Prior to anodising, the samples were ultrasonically degreased in acetone, rinsed in deionised water and dried under a cool air stream. The area of the samples exposed to the solution during anodising was 1 cm^2. The anodising process was performed using a Biologic SP-300 potentiostat. Potentiodynamic and potentiostatic anodising were carried out to study the effect of anodising on the alloy surface. The experimental set-up comprised a three-electrode cell arrangement, with the samples for anodising as working electrodes, a platinum wire as the counter electrode, and an Ag/AgCl (KCl saturated) as the reference electrode (RE).

The anodising bath, tartaric-sulfuric acid (TSA), was composed of 0.53 mol L^{-1} tartaric acid and 0.46 mol L^{-1} sulfuric acid, and the process was carried out at 37°C. A similar composition of this solution is used industrially in commercial tartaric-sulfuric anodising processes [101].

Potentiodynamic polarisation was carried out from open circuit potential (OCP), -0.35 ± 0.02 V, up to 14 V (vs. RE), with a sweep rate of 1 V min^{-1}. The effects of the anodising process on the surface and constituent particles were also studied by potentiostatic polarisation using several AA2024-T3 and AA2198-T8 samples. For this purpose, potentiostatic polarisation in the TSA solution was carried out at various potentials (−0.25, 0, 0.25, 1, 2, 3, 4, 5, 6, 7, 8, 9, 10, 11, 12, 13 and 14 V) vs. REF for 5 min. Charge densities for the potentiostatic polarisation curves were estimated directly from the EC-Lab® software using integration intervals of 3 s – 300 s, which correspond to the initial 3 s from the beginning of the polarisation to the end of the test. For each potential, the measurement was performed three times in order to obtain the average and deviation. In this paper a representative curve is presented in Figure 7. All the results can be found as supplementary material.

Images of the surfaces of the samples, before and after anodising, were taken using TM 3000 scanning electron microscope equipped with an EDX detector. The surface topography of both alloys was also analyzed by AFM and optical profilometer using a Nanoscope III MultiMode atomic force microscope instrument and a ZESCOPE model, respectively. The acquired AFM images were detected with non-contact mode cantilevers with a resonance frequency of 75 kHz and a spring constant of 2.8 N m^{-1} under an air environment. The measurements were performed at room temperature and humidity values between 30 and 55%.

Results

Potentiodynamic polarisation anodising

Typical potentiodynamic polarisation curves for the AA2024-T3 and AA2198-T8 alloys in tartaric-sulfuric anodising solution, from OCP, −0.35 V (vs. RE), to 14 V (vs. RE), are shown in Figure 1. The curves related to the two alloys showed different behaviours Figure 1(a). For the AA2198-T8 alloy, no peaks were observed. For the AA2024-T3, two peaks were observed, one between −0.1 V (vs. RE) and 0 V (vs. RE), (Figure 1(b)) and another between 4 V (vs. RE) and 6 V (vs. RE), (Figure 1(c)). These peaks resulted from the preferential oxidation of each type of micrometric particle in the alloy during potentiodynamic anodising. The oxidation potential corresponding to each particle is associated with its unique chemical composition and structure. It is important to highlight that this behaviour was previously observed in the AA2024-T3 alloy during potentiodynamic polarisation [64–67].

It is noteworthy that, after potentiodynamic polarisation (Figure 1), the surfaces of both alloys were examined, as shown in Figure 2. It is clear that in both alloys, voids were formed during the anodising process due to the onset of a preferential attack of the particles. At higher magnifications, as shown in regions 1 and 2, it is observed that these voids cause discontinuity in the formed oxide. Further details of the characteristics of these cavities were obtained through an optical profilometer, as shown in Figure 3.

Figure 3(a) presents images obtained by profilometry of both alloys after potentiodynamic polarisation in TSA. Bright spots are related to cavities formed due to IM dissolution. The average depth of the cavities formed in both alloys was also evaluated, as shown in Figure 3(b). Average values of (2.2 ± 0.8) µm and (1.8 ± 1.1) µm were observed for the AA2024-T3 and AA2198-T8 alloys, respectively. The depth profiles corresponding to some cavities presented in Figure 3(a) are also shown in Figure 3(c).

The profiles highlight the formation of cavities in the film surface, as well as the formation of imperfections above the cavities (indicated by the red arrows). According to Fratila-Apachitei et al. [102] and Moon et al. [103,104], these depressions are formed due to the differences in chemical composition between the particles and the matrix. At higher resolution, these features become more evident, as shown by the results obtained using AFM technique for the AA2024-T3 alloy in Figure 4. In fact, the dissolution of IMPs causes

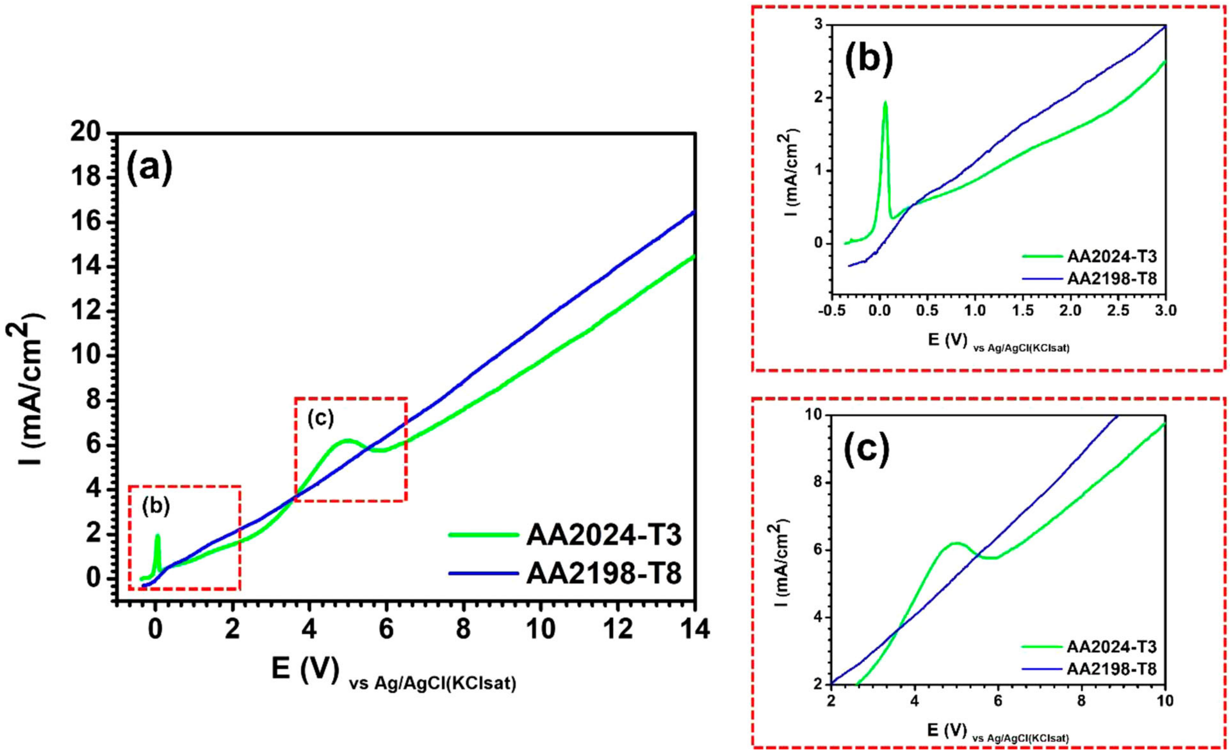

Figure 1. (a) Potentiodynamic polarisation curves of the AA2024-T3 and AA2198-T8 alloys obtained in 0.53 mol L^{-1} tartaric acid and 0.46 mol L^{-1} sulfuric acid (TSA) solution at 37°C carried out from OCP up to 14 V (vs. RE) with a scan rate of 1 Vmin^{-1}. (b and c) Higher magnifications of the dashed squares in (a).

discontinuity in the anodic film, and these irregularities are in agreement with the results reported by Ma et al. [82]. Besides, according to the authors, these irregularities act as preferred sites for corrosion propagation by favouring the contact between the substrate and the corrosive environment.

It is important to point out that dissolution of intermetallic particles during potentiodynamic polarisation (from the OCP up to 14 V (vs. RE)) is inevitable, as shown in Figure 5 where the interface between the anodised and non-anodised surfaces for both alloys is identified. The blue arrows point to the IMPs on the unexposed surfaces, while the red ones point to the formed cavities on the surfaces exposed to the electrolyte. The formation of cavities is associated with the dissolution of IMPs. The anodised area and its boundaries are clearly identified by EDX maps, as shown in Figure 6, where the anodised region presents higher oxygen content, when compared to the non-anodised region.

The cause of the peaks observed in the AA2024-T3 alloy, as well as the influence of voltage on the dissolution of particles in both alloys, is investigated in the following section.

Potentiostatic polarisation anodising and charge effect

Figure 7 shows the current density-time data recorded during the anodising of the studied alloys under different constant voltages. The curves show a fast current density drop in the first seconds, which is typical of the barrier layer formation. The subsequent increase in current and the current density peak followed by current stabilisation are related to the growth of the porous layer – associated with the steady-state [105,106].

The curves of both alloys indicate that the greater the potential, the higher the current density and the faster the initiation of porous layer growth. This is observed by

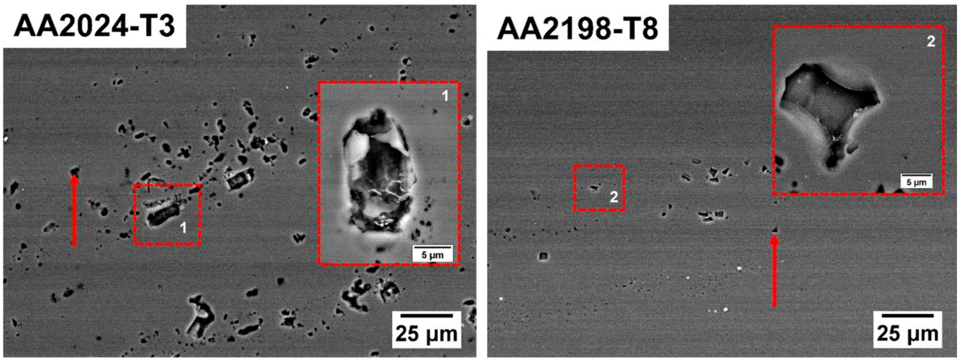

Figure 2. Backscattered electron micrographs of the AA2024-T3 and AA2198-T8 alloys surface after potentiodynamic polarisation in TSA solution at 37°C, from the OCP up to 14 V (vs. RE). The red arrows indicate the voids on the surface resulting from the dissolution of the micrometric particles.

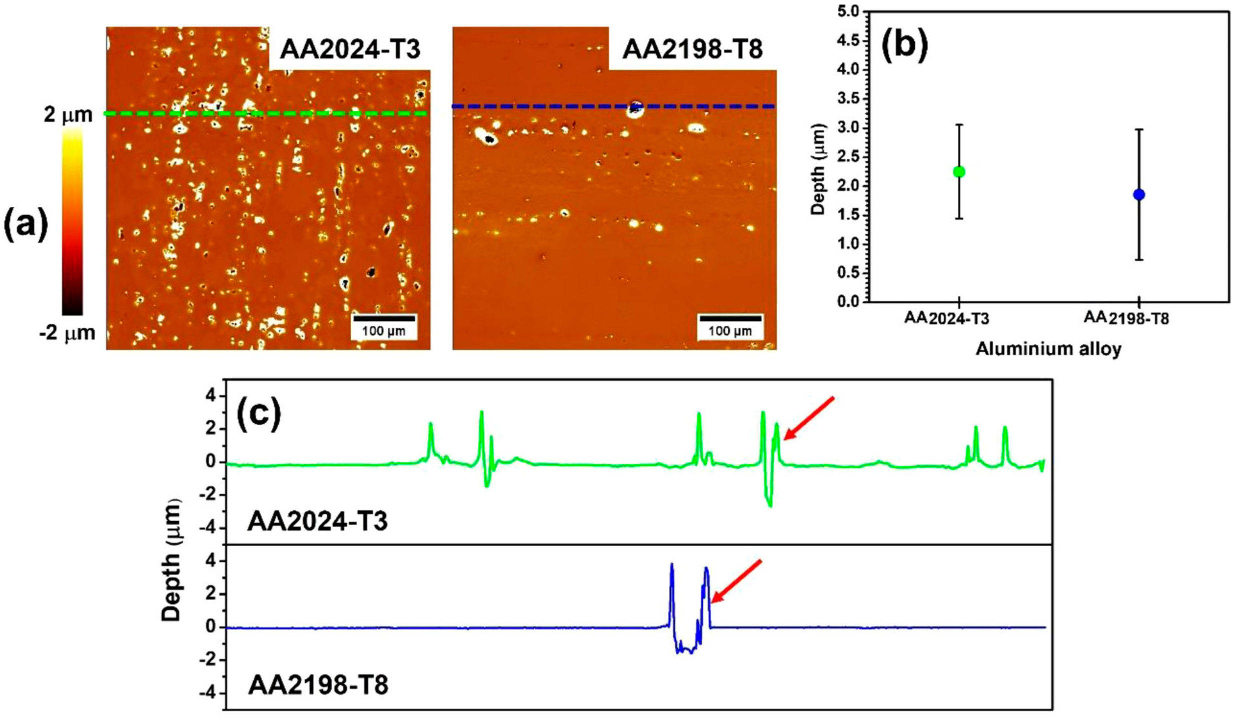

Figure 3. (a) Optical profilometry images of the AA2024-T3 and AA2198-T8 alloys after potentiodynamic polarisation in TSA from the OCP up to 14 V (vs. RE). (b) The average size of the voids on the surface of both alloys caused by the dissolution of micrometric particles during polarisation. (c) Profiles corresponding to the figure (a). The red arrows in (c) indicate surface defects caused by the dissolution of micrometric particles.

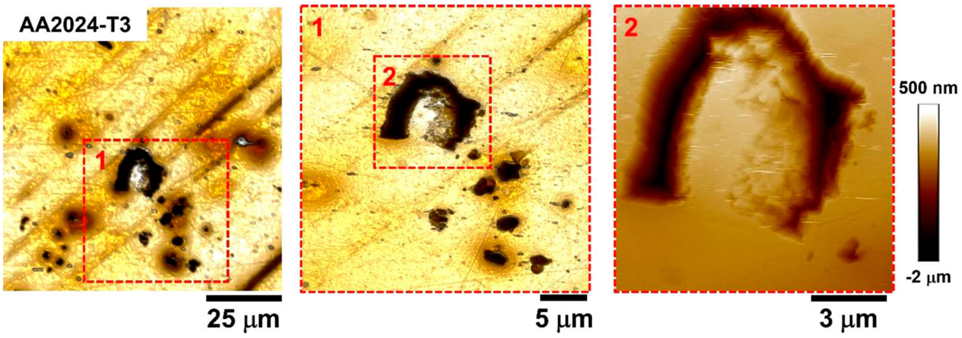

Figure 4. AFM surface topography of AA2024-T3 alloy surface after potentiodynamic polarisation in TSA from the OCP up to 14 V (vs. RE).

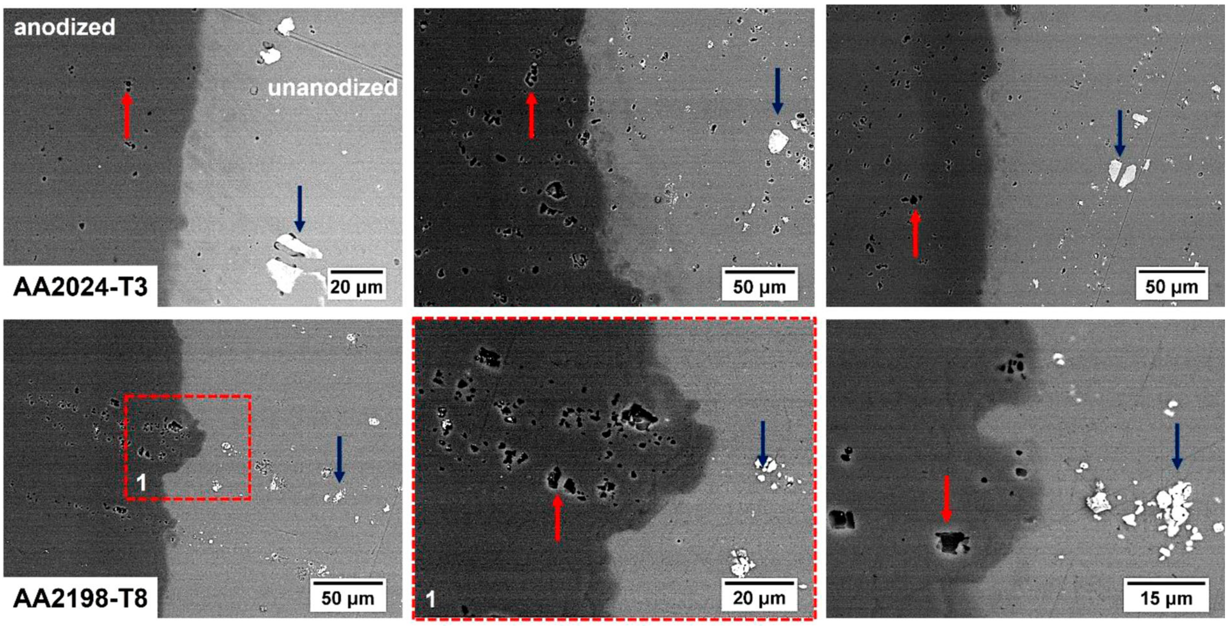

Figure 5. Backscattered electron micrographs of the AA2024-T3 and AA2198-T8 alloys surface after potentiodynamic polarisation in TSA solution at 37°C, from the OCP up to 14 V (vs. RE). The red and blue arrows indicate surface voids caused by the dissolution of micrometric particles and micrometric particles that did not have contact with the anodising bath, respectively.

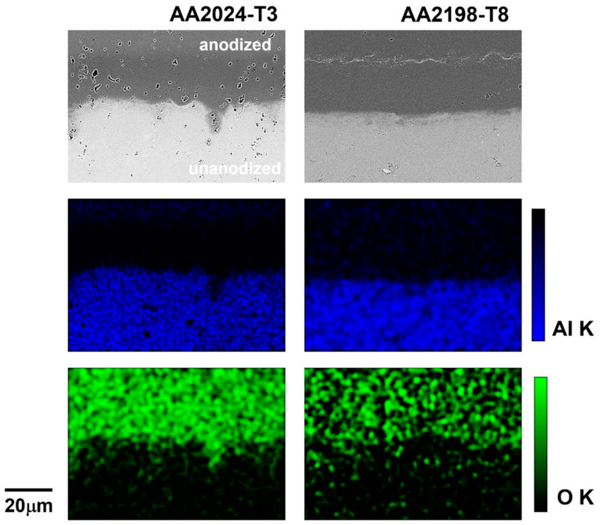

Figure 6. Energy-dispersive X-ray spectroscopy maps showing the distribution of the detected elements on the interface between the anodised and unanodised surface for both alloys, AA2024-T3 and AA2198-T8.

the faster occurrence of the peaks as potential increases. The exception to this behaviour is at 0 V (vs. RE), for the AA2024-T3 alloy, where the curve presents a peak of current density earlier than that observed for the other tested potentials. This potential is related to the dissolution of IMPs [65]. The charge density was estimated by integration of the area underneath the potentiostatic curves shown in Figure 7. Figure 8 shows a tendency of the charge density to increase with applied voltage, although this increase is not linear. The charge densities for both tested alloys were similar up to 8 V (vs. RE), but for greater applied voltages, the charge density values were appreciably higher for the AA2024-T3 compared to the AA2198-T8.

According to Curioni et al. [65], potentiostatic studies provide important information during anodising, and in our study, potentiostatic anodising was also carried out. After potentiostatic anodising at different voltages, the behaviour of the intermetallic particles was investigated by surface examination using scanning electron microscopy (SEM), before and after anodising. Surface examination after anodising allowed a correlation between the electrical response of the second-phase particles and the results presented in Figures 1, 7, and 8.

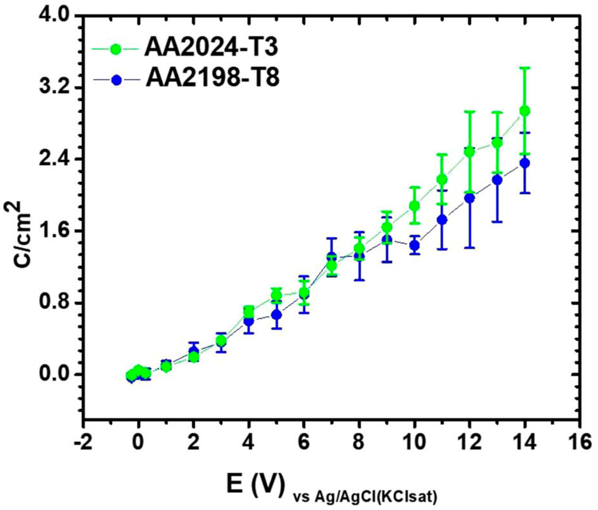

Figure 8. Plots showing charge potential relationship in the AA2024-T3 and AA2198-T8 alloys potentiostatically polarised (vs. RE) for 5 min in TSA solution.

The behaviour of coarse intermetallic particles (IMPs) during anodising

Potentiostatic polarisation of both studied alloys in the TSA solution was carried out for 5 min at potentials of −0.25 V (vs. RE) , 0 V (vs. RE), and 0.25 V (vs. RE), and the results are shown in Figure 9. According to and Zhou et al. [107] and Saenz de Miera et al. [66], at potentials near the OCP, an oxide with very poor adhesion to the metal and voids at the metal/film interface can be observed. As observed in Figure 10, at the polarisation potential corresponding to −0.25 V (vs. RE), IMPs attack were not observed for both alloys, whereas, at 0 V (vs. RE), total dissolution of the IMPs was observed for the AA2024-T3 alloy. Interestingly, at 0.25 V (vs. RE), there was no attack or dissolution of the IMPs. Higher magnification images allowed the observation of some characteristics in both alloys after polarisation at certain voltages. Figure 10 displays the surface of the AA2024-T3 before and after potentiostatic polarisation in TSA, where an attack (trenching) was observed around the particles at various potentials, but at 0 V (vs. RE), the IMPs dissolved completely, as shown in Figure 11. It is known that the AA2024-T3 alloy presents different types of particles in its microstructure which are composed mainly of Al-Cu-Mg and Al-Cu-Fe-Mn. Both particles dissolved at 0 V (vs. RE). At this potential, the AA2198-T8 alloy only showed

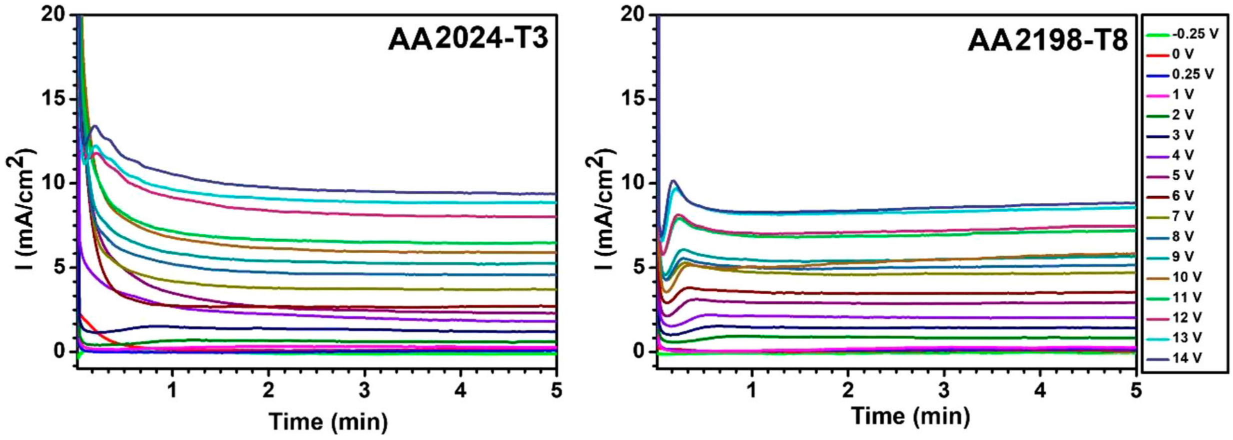

Figure 7. Current density-time response during polarisation of the AA2024-T3 and AA2198-T8 alloys in TSA solution at – 0.25 V to 14 V (vs. RE) at 37°C, for 5 min.

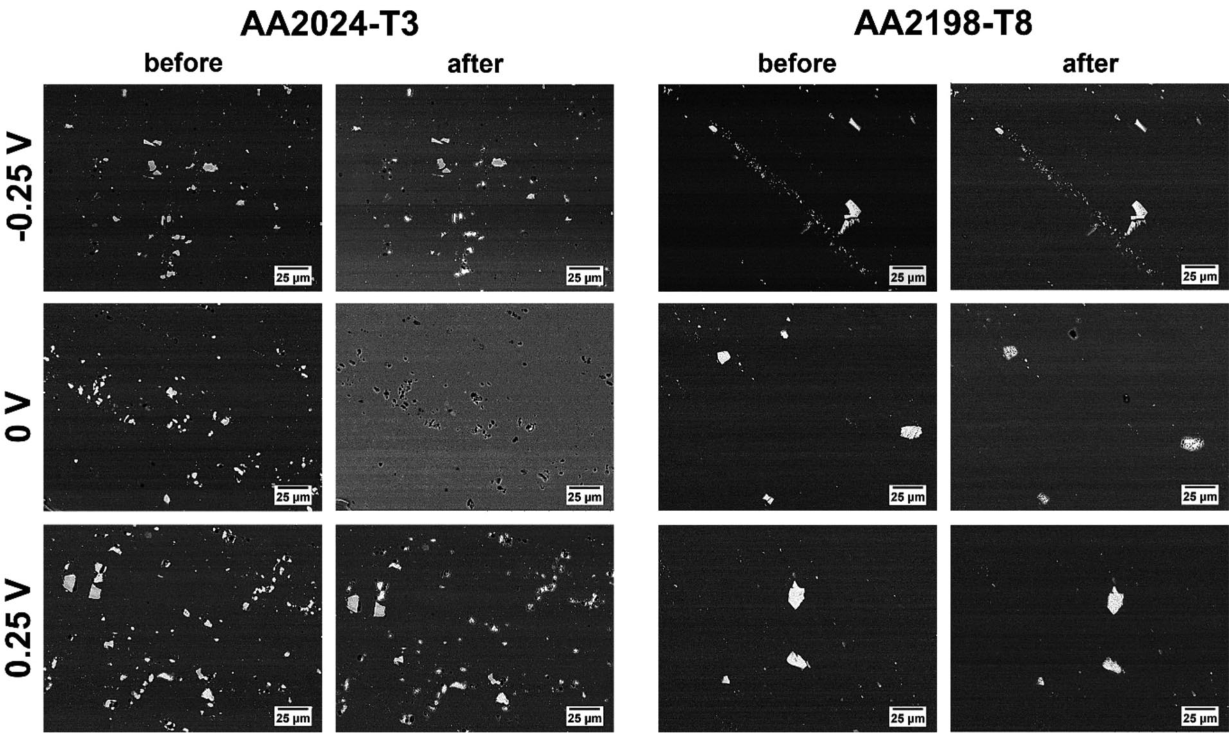

Figure 9. Backscattered electron micrographs showing the AA2024-T3 and AA2198-T8 alloys surface before and after potentiostatic polarisation in TSA for 5 min at − 0.25, 0 and 0.25 V (vs. RE).

partial dissolution of IMPs (which are mainly Al-Cu-Fe particles) (Figure 12).

At voltages corresponding to 1 V (vs. RE), 2 V (vs. RE) and 3 V (vs. RE), different behaviours are observed for both alloys, as Figure 13 shows. At 1 V (vs. RE) and 2 V (vs. RE), there was no dissolution of any IMPs for both alloys, but at 3 V (vs. RE) differences in the behaviour of the IMPs were observed. At this voltage, the Al-Cu-Fe-Mn particles in the AA2024-T3 alloy undergo partial dissolution, whereas the Al-Cu-Mg ones showed total dissolution (Figure 14(a)). Figure 14(b) confirms this observation showing, respectively, the complete and partial dissolution of these particles. At 3 V (vs. RE), the AA2198-T8 showed different characteristics (Figure 15). Partial dissolution of the isolated IMPs was observed, as shown by the yellow arrows in Figures 15(a,b), while the clustered particles showed superficial attack, Figures 15(c,d). At higher applied voltages, new characteristics were observed, as shown in Figure 16, which corresponds to 4 V (vs. RE), 5 V (vs. RE) and 14 V (vs. RE). From 4 V (vs. RE) onwards, all IMPs in the AA2024-T3 alloy were dissolved, while in the AA2198-T8 alloy, dissolution only occurred at potentials above 5 V (vs. RE). At 4 V (vs. RE), the IMPs in the AA2198-T8 alloy were partially dissolved, as evident in Figure 17. Figure 17(a) shows that at a potential of 4 V (vs. RE), some particle clusters were not fully dissolved (remnants of IMPs were indicated by the yellow arrows, Figure 17(b,c)).

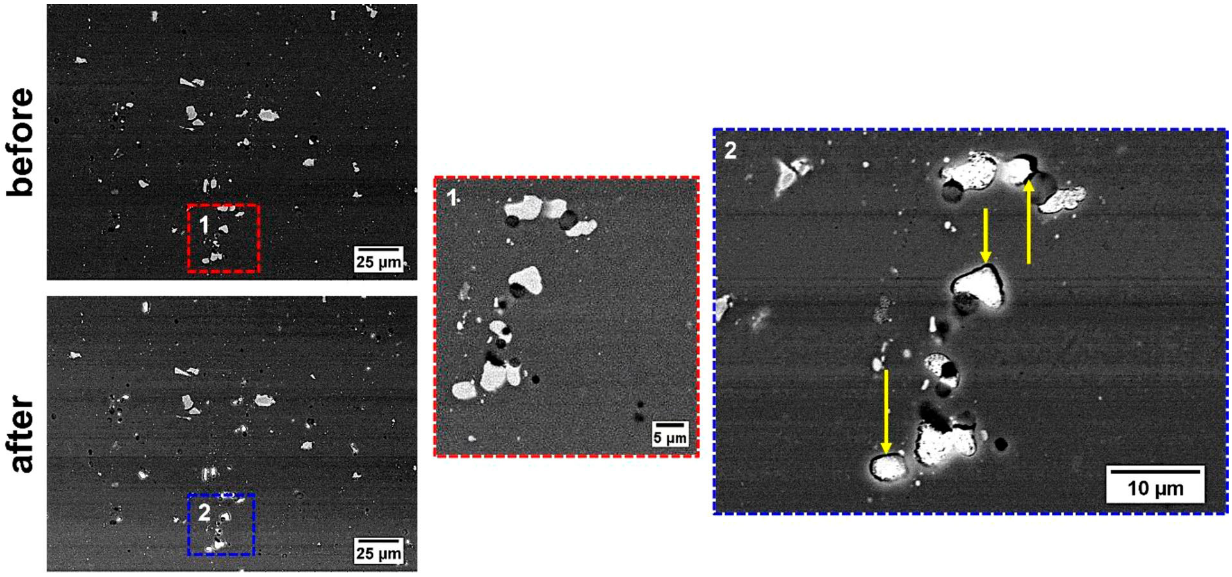

Figure 10. Backscattered electron micrographs showing the AA2024-T3 alloy surface before and after potentiostatic polarisation in TSA for 5 min at − 0.25 V (vs. RE). The red and blue dashed squares show higher magnification of the regions highlighted before and after anodising. The yellow arrows indicate the trenching between micrometric particles/matrix alloy.

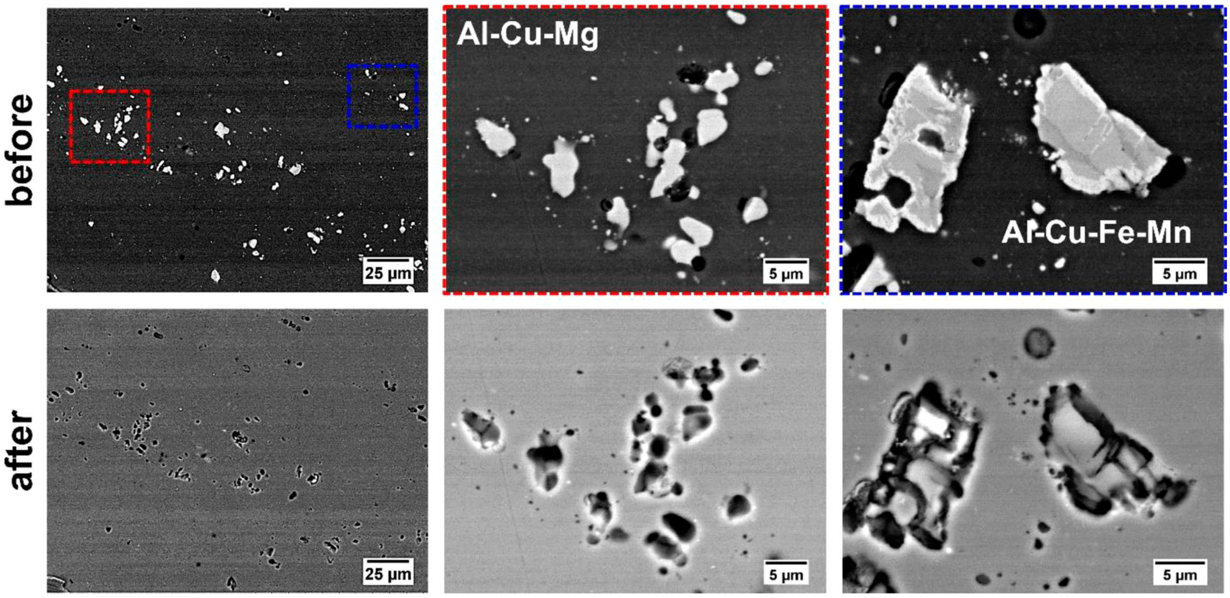

Figure 11. Backscattered electron micrographs showing the AA2024-T3 alloy surface before and after potentiostatic polarisation in TSA for 5 min at 0 V (vs. RE).

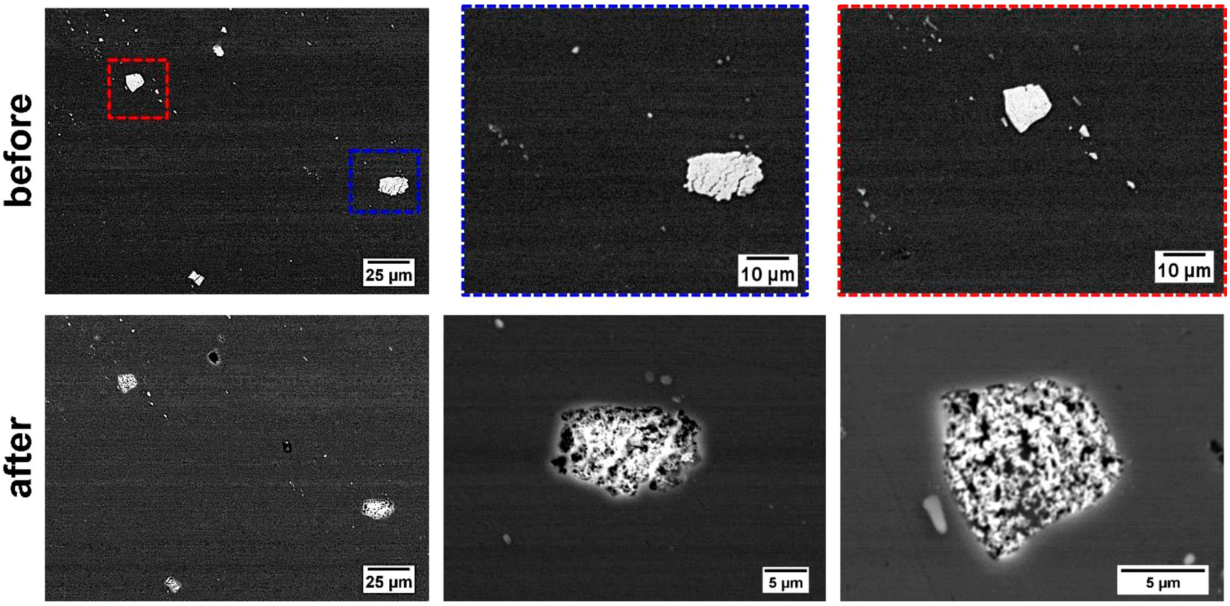

Figure 12. Backscattered electron micrographs showing the AA2198-T8 alloy surface before and after potentiostatic polarisation in TSA for 5 min at 0 V (vs. RE). The red and blue dashed squares show higher magnification of the regions highlighted before anodising.

It is noteworthy that, at potentials typical of the industrial condition (14 V (vs. RE)), all IMPs in both alloys dissolved (Figure 18). Polarisation was performed for a short period (5 s), therefore the anodic layer was not too thick. This method was used to favour examination of the alloy surface after anodising. The results showed that in the industrial condition, even in the first seconds, the IMPs can be totally dissolved in the bath (Figure 19).

Discussion

It is well known that the coarse intermetallic particles (IMPs) are formed in the Al-alloys during casting due to the low solubility of some elements, mainly Fe. These particles are of micrometric scale and can be found isolated or in clusters on the alloy surface. They result in discontinuity of the passive film in Al and, depending on their chemical composition, act as anodic or cathodic sites relative to the matrix favouring initiation of the corrosion process [108–110]. Thus, it is expected that IMPs react during anodising, as shown in Figure 5. Also, the presence of defects caused by the dissolution of IMPs (Figures 2, 4, and 5) can influence the propagation of corrosion in anodised alloys before the sealing process [82]. Therefore, understanding the mechanism of dissolution of these IMPs during the anodising process is vital.

Recently, Araujo et al. [111] carried out a detailed study on the microstructural characteristics of the AA2024-T3 and AA2198-T8 alloys through microstructural and statistical analysis. The authors reported that the intermetallic particles in the AA2198-T8 alloy have very similar chemical compositions. Variations in the amount of Fe and Cu in these particles are not significant enough to characterise them into high, medium, or low Cu-containing particles, as performed by Ma et al. [75]. This shows that the studied alloy presents different

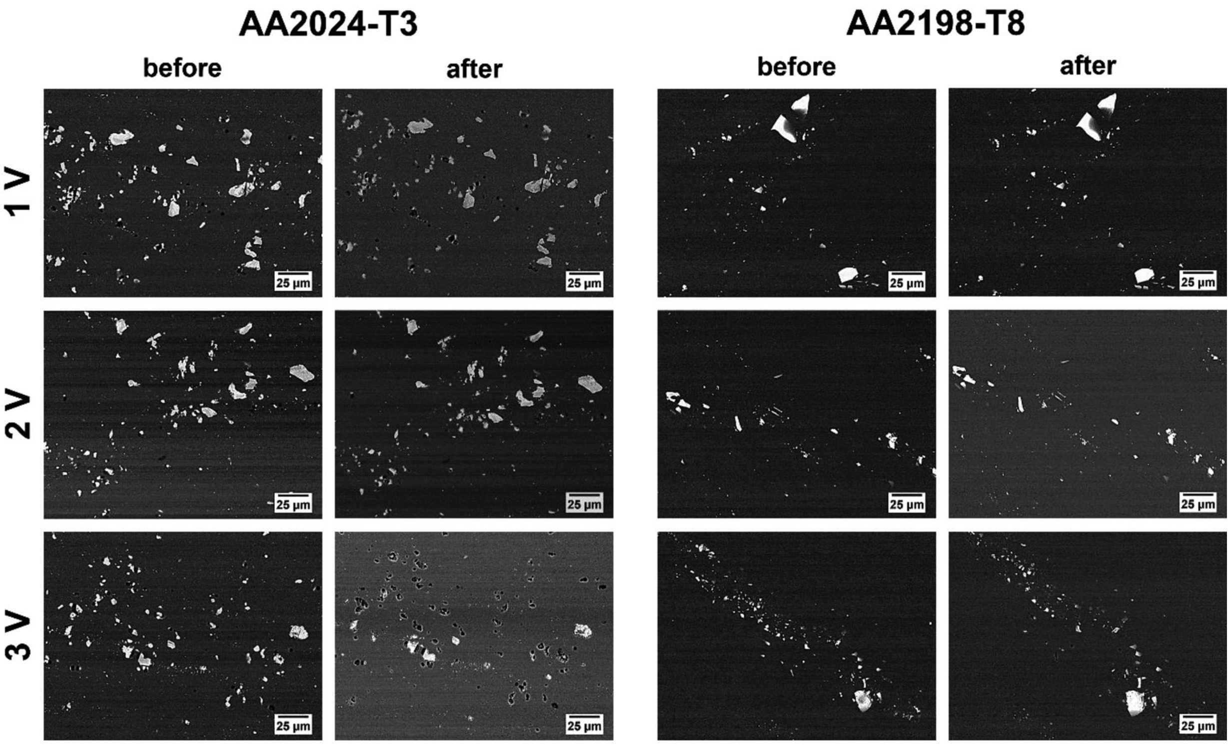

Figure 13. Backscattered electron micrographs showing the AA2024-T3 and AA2198-T8 alloys surface before and after potentiostatic polarisation in TSA for 5 min at 1, 2 and 3 V (vs. RE).

types of particles from those reported in previous works on the anodising of Al-Cu-Li alloys [75,80,81,112]. For the AA2024-T3 alloy, different particles were observed with different Cu-Fe contents, namely, AlCuFeMnSi, AlCuMg and AlCuFeMgMn.

These results indicate that the behavior of the particles in the AA2198-T8 alloy during the potentiodynamic and potentiostatic anodising processes are similar, since, in this alloy, the IMPs have only Cu and Fe in their composition. Therefore, different particle oxidation behaviours are

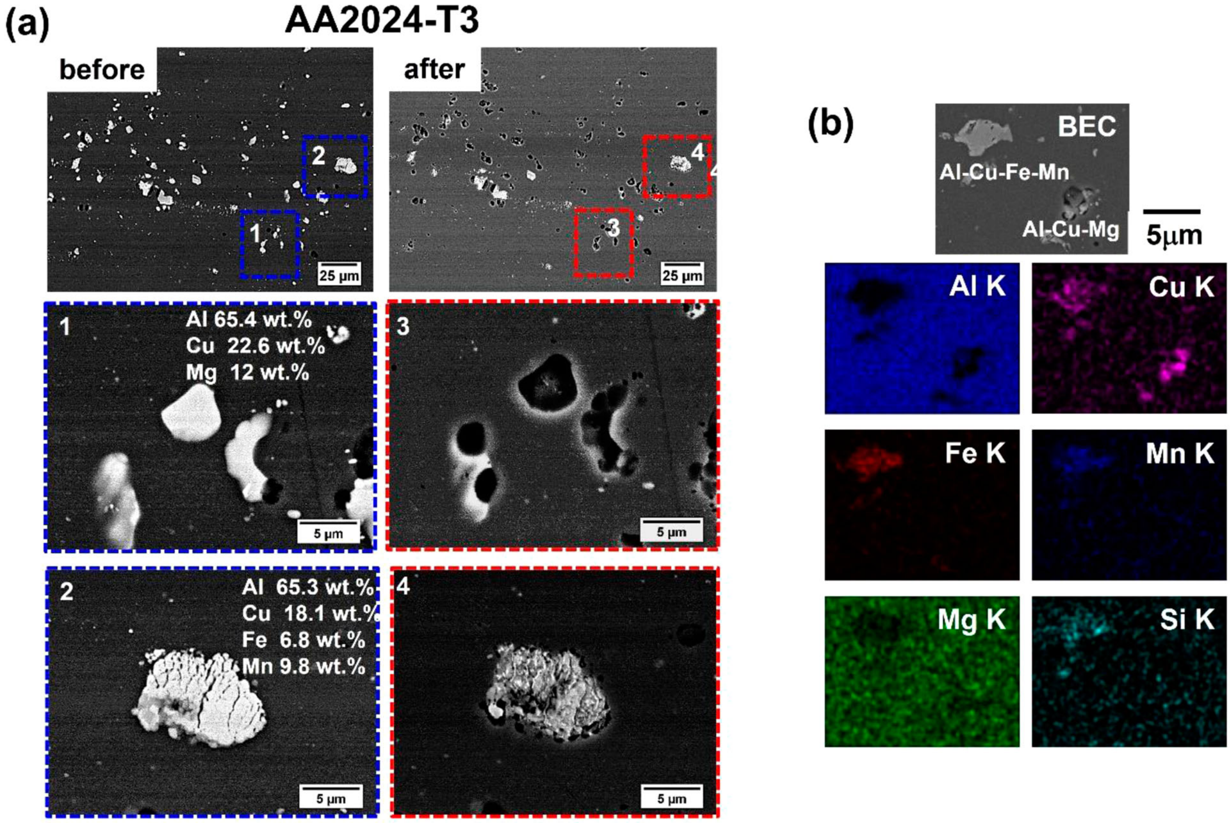

Figure 14. (a) Backscattered electron micrographs showing the AA2024-T3 alloy surface before and after potentiostatic polarisation in TSA for 5 min at 3 V (vs. RE). (b) Energy-dispersive X-ray spectroscopy maps obtained after potentiostatic polarisation in TSA for 5 s at 3 V (vs. RE). The red and blue dashed squares show higher magnification of the regions highlighted before and after anodising.

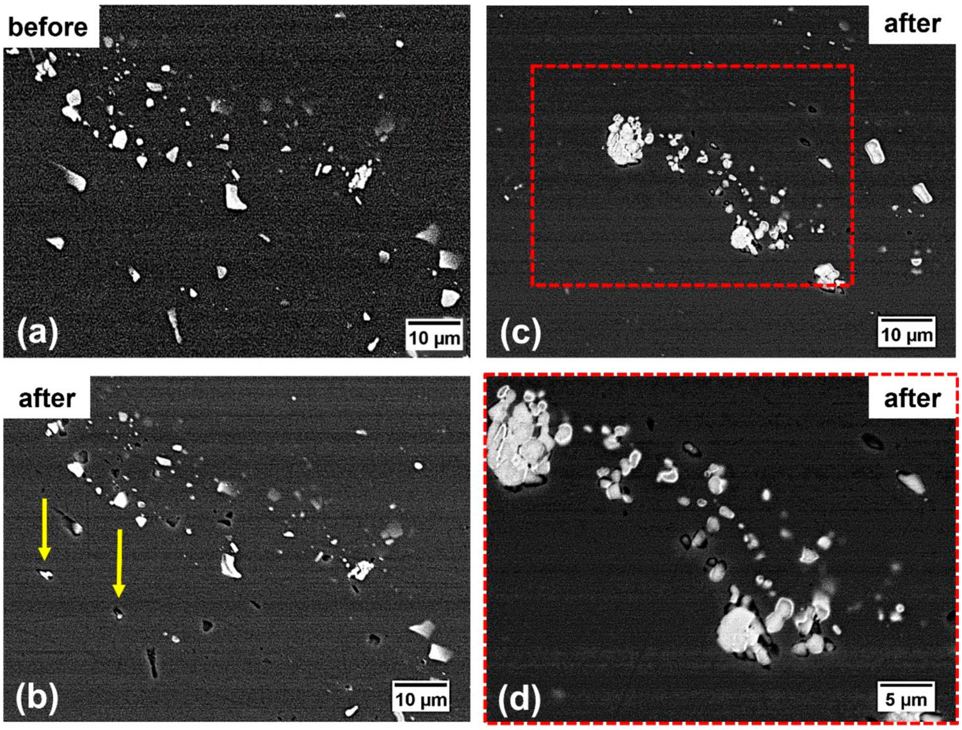

Figure 15. Backscattered electron micrographs showing the AA2198-T8 alloy surface before and after potentiostatic polarisation in TSA for 5 min at 3 V (vs. RE). (a and b) Images from the same regions before and after the potentiostatic polarisation. (c) Images from another region after potentiostatic polarisation. (d) Higher magnification of the region highlighted in (c). The yellow arrows in (b) indicate the partial dissolution of the micrometric particles.

expected during anodising of the AA2024-T3 compared with the AA2198-T8. Figure 20 summarises the behaviour of coarse particles during anodising in TSA solution.

According to Araujo et al. [111], the AA2024-T3 alloy presents a larger density of particles than the AA2198-T8 alloy, and this can affect the voltage–current response. It can also explain the peak observed at 0 V for the AA2024-T3 alloy (Figure 1). It is important to highlight that potentiostatic anodising performed at 0.25 V (vs. RE) does not result in particle dissolution, whereas dissolution was observed when potentiostatic polarisation was conducted at 0 V (vs. RE). This result confirms that the peak at 0 V (vs. RE) corresponds to the oxidation potential of the constituent particles in the AA2024-T3 alloy. The attack occurred both on clustered and isolated IMPs, supporting the fact that the current peak at 0 V (vs. RE) is due to

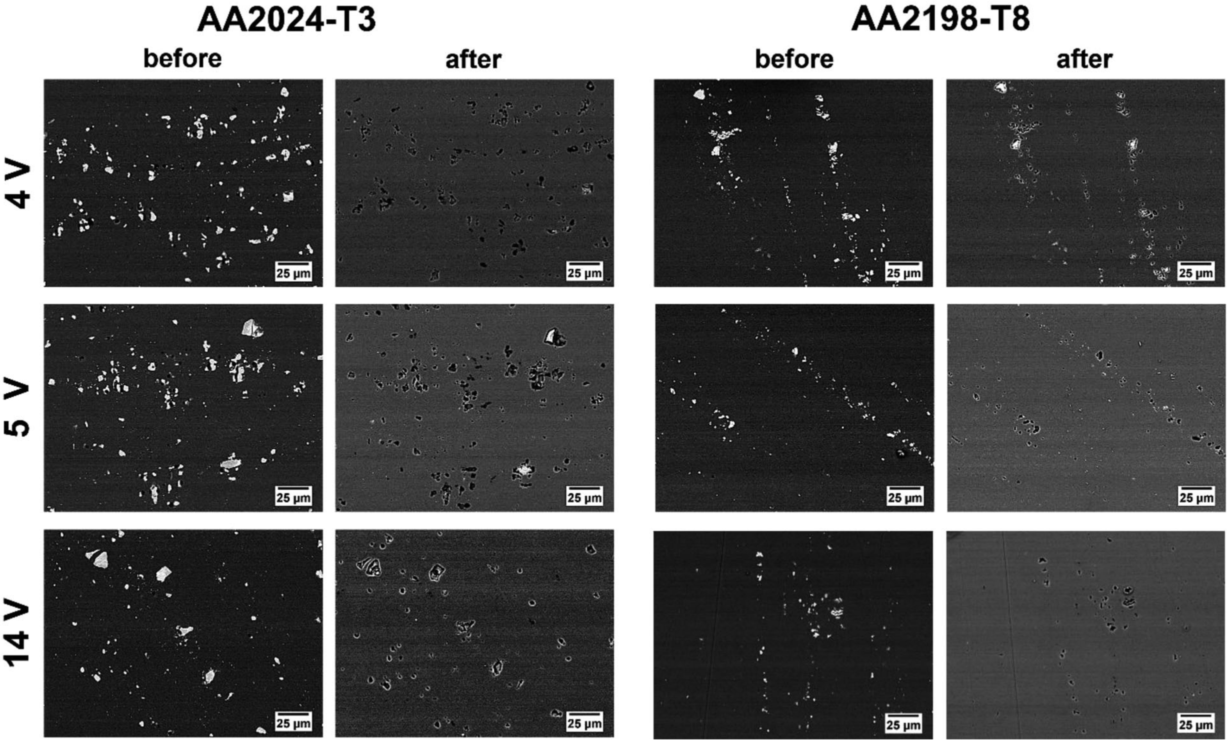

Figure 16. Backscattered electron micrographs showing the AA2024-T3 and AA2198-T8 surface before and after potentiostatic polarisation in TSA for 5 min at 4, 5 and 14 V (vs. RE).

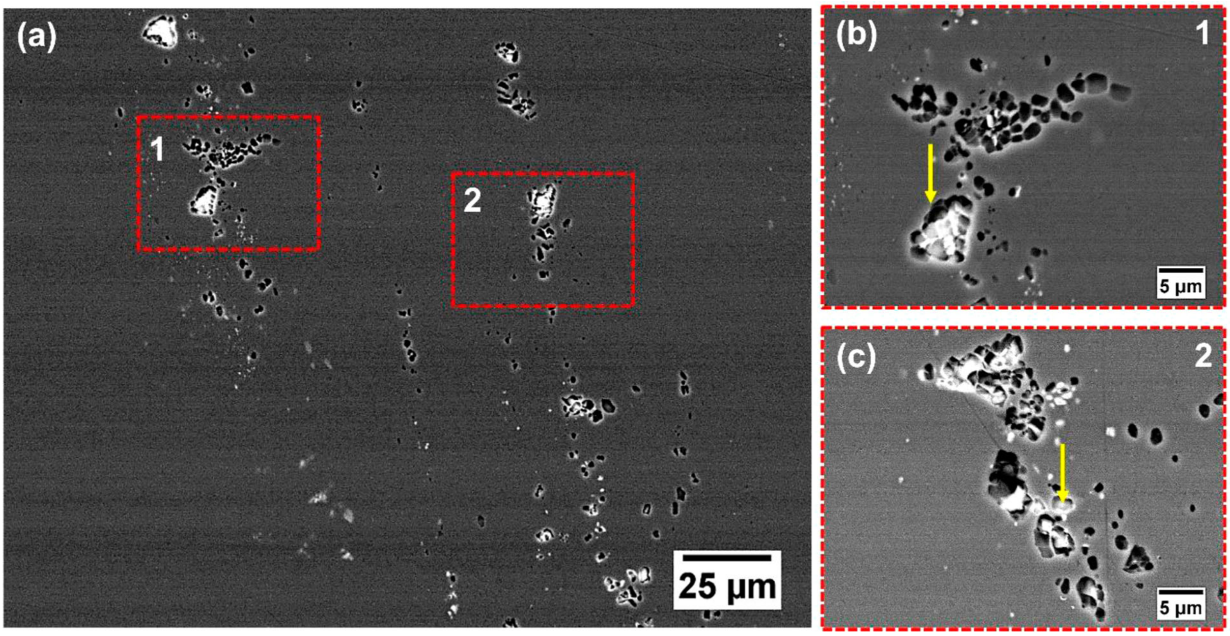

Figure 17. Backscattered electron micrographs showing the AA2198-T8 alloy surface before and after potentiostatic polarisation in TSA for 5 min at 4 V (vs. RE). (a) Panoramic image. (b and c) Higher magnification of the scares highlighted in (a). The yellow arrows in (b) and (c) indicate the residual particles.

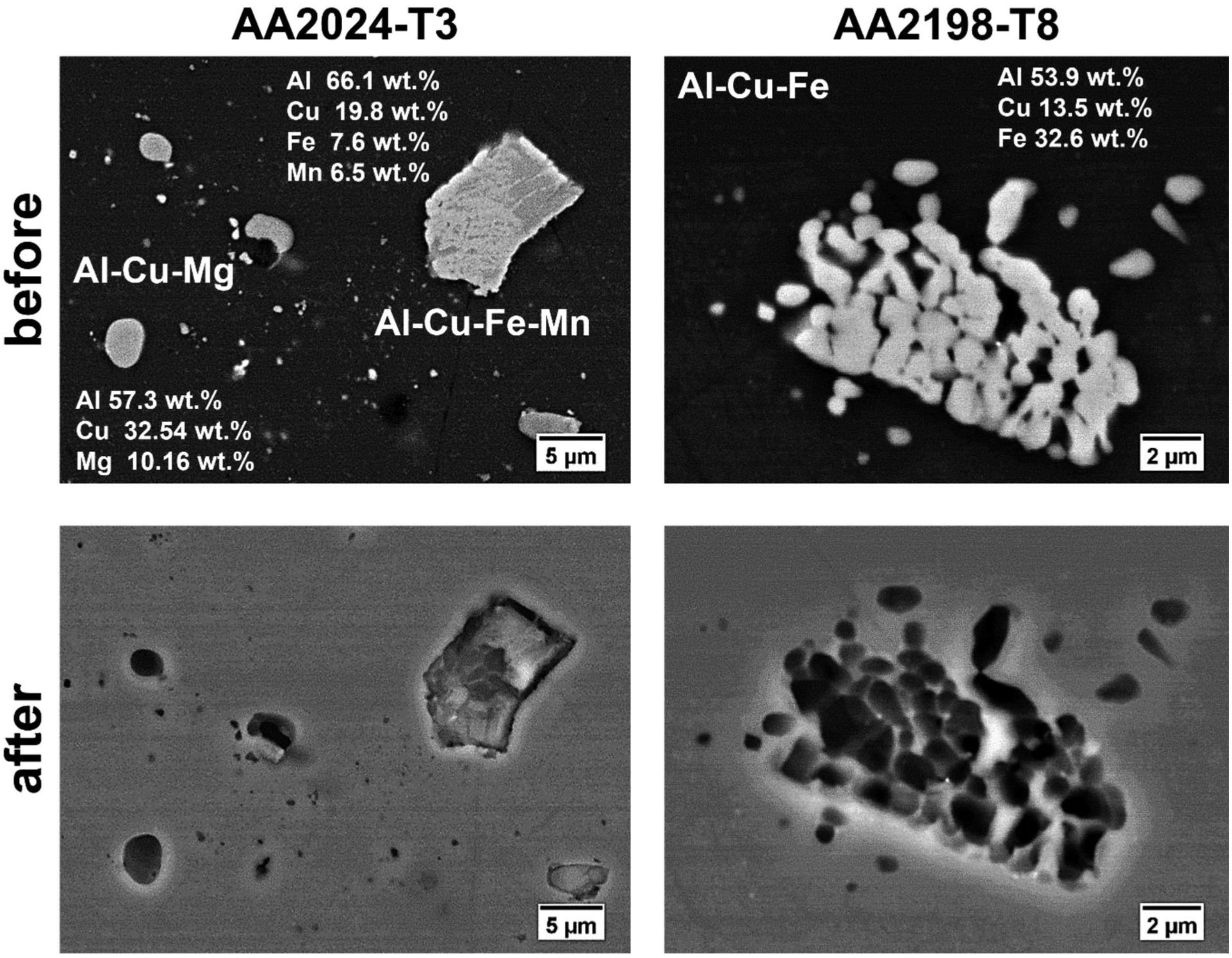

Figure 18. Backscatter electron micrographs showing the AA2024-T3 and AA2198-T8 alloys surface before and after potentiostatic polarisation in TSA for 5 min at 14 V (vs. RE).

the oxidation of the constituent particles (Figure 11). Interestingly, partial dissolution of IMPs in the AA2198-T8 alloy was observed in samples polarised in TSA at 0 V (vs. RE) (Figure 12).

The differences in the anodising behaviour of the IMPs present in both alloys at −0.25 V (vs. RE), 0 V (vs. RE) and 0.25 V (vs. RE) can be associated with the differences in chemical composition. As mentioned for the AA2024-T3

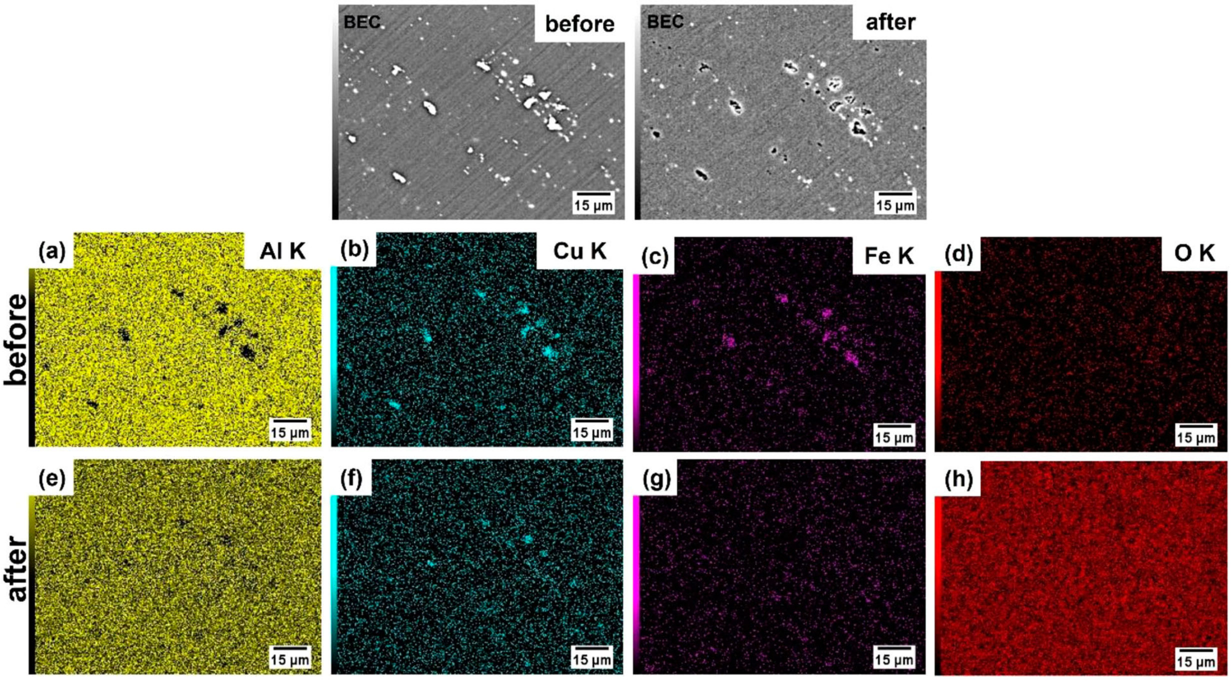

Figure 19. Energy-dispersive X-ray spectroscopy maps of the corresponding SEM micrographs obtained before (a–d) and after (e–h) potentiostatic polarisation in TSA for 5 s at 14 V (vs. RE) showing the dissolution of intermetallic particles after anodising.

alloy, potentiostatic polarisation at −0.25 V (vs. RE) and 0.25 V (vs. RE) resulted in matrix trenching without particles dissolution, but the particles were dissolved at 0 V (vs. RE). Curioni et al. [64] observed that after polarisation of the AA2024-T3 alloy at 0.2 V (vs. RE), cavities had been generated close to clusters of second-phase particles. The EDX analyses performed on these particles revealed Al: Cu ratios close to 1, and magnesium remnants, suggesting that the cavities were generated by the preferential dissolution of high magnesium content particles. This behaviour is explained by the high solubility of magnesium oxide in the acidic electrolyte. The high anodic activity of the Mg-rich phases at low overpotentials has already been reported by Liu et al. [113]. This explains the fact that at low potentials (−0.25 V (vs. RE)/ 0.25 V (vs. RE)), this behaviour is not observed for the IMPs present in the AA2198-T8 alloy since the IMPs are enriched only in Cu and Fe.

For the AA2024-T3 alloy, at 0 V (vs. RE), all IMPs were dissolved. As already mentioned, the peak on the potentiodynamic curve in Figure 1(b) corresponds to this voltage. The

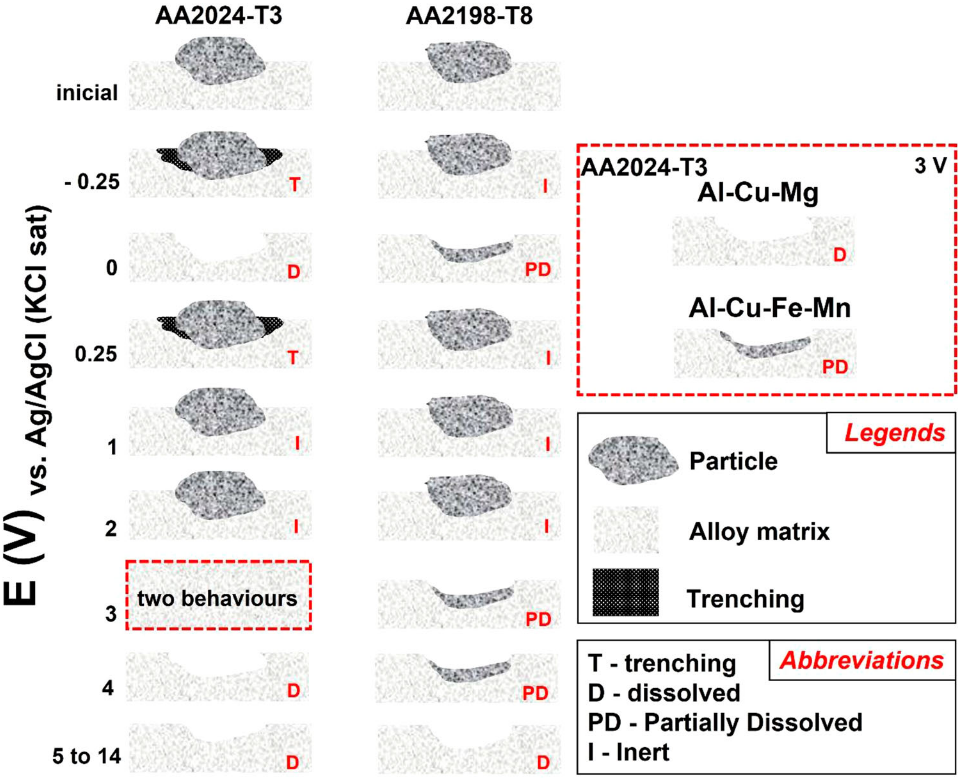

Figure 20. Schematic diagram of the behaviour of the intermetallic particles during the anodising process in TSA solution at 37°C.

dissolution of the IMPs at this voltage is associated with the Cu present in these particles, which leads to a higher rate of oxygen evolution on the IMPs. This behaviour was extensively explored by Mirnaly Saenz de Miera in his Ph.D. thesis [114], when studying the anodising behaviour of the AA2024-T3 alloy in sulfuric and chromic acid and had already been reported by Sepulveda et al. [115] and Moutarlier et al. [116]. It is worth mentioning that the AA2024-T3 alloy presents higher percentage of IMPs per area compared to the AA2198-T8 alloy, about four times more [111].

At 0 V (vs. RE), some particles in the AA2198-T8 alloy were partially dissolved. In fact, according to Araujo et al. [11], the Cu / Fe ratio of the IMPs present in the AA2198-T8 alloy can vary between 2 and 4. It is reported [80] that the IMPs with higher Cu/Fe ratio tend to have higher Li content. Although, in this work, it was not possible to detect Li in the IMPs due to the low resolution of the EDX for the detection of this element, Ma et al. [75] suggested in one of their works that in Al-Cu-Li alloys, IMPs containing high Cu content tend to have a higher percentage of Li. Years later, MacRae et al. [117] confirmed this hypothesis using electron and proton microprobes in parallel with energy-dispersive X-ray spectrometry and soft X-ray emission spectroscopy (SXES), when characterising the AA2099-T8 alloy.

It is understood that IMPs with high Cu content tend to promote an additional driving force for the selective dissolution of Al, Fe and Li, of the IMPs during anodisation at 0 V (vs. RE), which results in their partial dissolution, as observed in Figure 12. Also, according to Saenz de Miera et al. [63], Mg-enriched second phases have been reported to be more readily oxidised compared with Cu-Fe enriched phases. This was also attributed to the absence of a stable oxide above Mg-enriched particles which results in direct metal dissolution. Therefore, AA2198-T8 particles are also partially dissolved at 0 V (vs. RE) due to their slow dissolution rate and size.

It is important to highlight that the partial dissolution of IMPs at 0 V during potentiostatic polarisation in Al-Cu-Li alloys was also reported by Liu et al. [81] and Wu et al. [80], when studying the AA2219 and AA2099 alloys during anodisation in adipic-sulfuric and tartaric-sulfuric acid solution, respectively.

It is interesting to observe that between 3 V (vs. RE) and 4 V (vs. RE) the current density difference is almost twice that between the other tested potentials, for both alloys (Figure 8). This can be explained by a large number of particles attacked at 4 V (vs. RE) besides the increased attack of particles (Figures 14–17). The increment in charge density with the applied potential is mainly related to the thickening of the anodised layer, but also the dissolution of the IMPs. However, the charge density associated with dissolution represents a minor contribution, since the results of polarisation at 1 V (vs. RE) and 2 V (vs. RE) did not show evidence of particle dissolution in both alloys. However, the charge density presented a significant increase as the potential increased. Although there is no direct connection between charge density and particle dissolution, the current density values related to polarisation at 0 V (vs. RE) (for the AA2024-T3 alloy) and the large increase in charge density from 3 V (vs. RE) to 4 V (vs. RE), which correspond to particle dissolution potentials, show that charge density is also affected by particle dissolution.

Ma et al. [75] showed that coarse constituent particles in the AA2099 alloy, with dissimilar compositions, present different behaviours during anodising, and this behaviour depends on the composition of the particles. Wu et al. [80] also studied the AA2099 alloy and observed that the dissolution potential of high-copper Al–Fe-Mn-Cu particles was close to 0 V, and copper-rich nanoparticles were formed at the sites, where the particles had been dissolved. On the other hand, Liu et al. [81] observed that in the AA2297-T8 alloy with particles with different Cu content, the high Cu-containing particles (HCCPs) were preferably dissolved at potentials around 0.1 V and completely dissolved at 3 V. This resulted in the absence of a stable oxide film and the presence of cavities in the film. The medium Cu-containing particles (MCCPs) were not dissolved at 0.1 V but were oxidised at 3 V, while the Cu-Mn-Fe-containing particles remained on the surface at potentials below 3 V and were dissolved at potentials above 3 V. The differences in the behaviour of the IMPs in the AA2099, AA2297 and the AA2198 are explained by differences in the alloy compositions. The AA2099 presents lower Cu and Ag content, but higher Li, Mn and Zr contents than the AA2198, whereas the AA2197 presents lower Cu and Mg contents but higher Li content, when compared to the AA2198 alloy.

Differences in the composition of Al-Cu-Li alloys (such as in Cu, Fe, Mn and Zn and Li [11]) lead to significant changes in the composition of the IMPs. In the present study, however, AA2198 presents only one type of IMP composed of Al, Cu and Fe with differences in size and distribution [11,111] with slight variation in composition. This shows that each Al-alloy presents its own characteristics and, consequently, an extensive study on the behaviour of coarse intermetallic particles of each of this kind of alloy deserves a proper investigation.

At potentials above 5 V (vs. RE), all particles dissolved in both alloys (see supplementary material). It is important to note that, for both alloys, under industrial anodising potential (14 V), 5 min of anodising resulted in the dissolution of the particles (Figure 18). The EDX results of the AA2198-T8 alloy (Figure 19) suggest that selective leaching of elementary components (such as Fe) in the particles possibly preceded the complete dissolution of the constituent particles at the beginning of anodising. This is under investigation and will be presented in future works on the AA2198 alloy, since the works by Curioni et al. [64] and Saenz de Miera et al. [65,66,118] have reported, in detail, the role of elements in IMPs for the AA2024 alloy during sulfuric acid and TSA anodising.

Conclusions

The IMPs in both alloys, AA2024-T3 and AA2198-T851, exhibited similar or different behaviours depending on the voltage applied during anodising. The AA2024-T3 alloy has two main types of IMPs, mainly composed of Al-Cu-Mg and Al-Cu-Fe-Mn; while the IMPs in the AA2198-T8 alloy are enriched in Cu-Fe, with slight variations in their chemical composition. A current peak related to the dissolution of IMPs was observed at 0 V (vs. RE) during the potentiodynamic polarisation of the AA2024-T3 alloy. For both alloys, full dissolution of IMPs does not occur at potentials in the range of 0 V (vs. RE) to 2 V (vs. RE), but at potentials above 3 V (vs. RE), these particles are visibly attacked. At 0 V (vs. RE), the IMPs in the AA2024-T3 alloy are attacked. Preferential dissolution of the constituent particles occurs at potentials close to or above 4 V (vs. RE) for the AA2024-T3 and at or above 5 V (vs. RE) for the AA2198-T8. For both alloys, the preferential attack of these particles occurs initially in the clustered particles. However, at potentials above 5 V (vs. RE), both types of particles, isolated or clustered, are attacked. The charge density values increased at potentials where the IMPs are attacked, showing that the current related to this attack has a significant contribution to the total charge density measured.

Disclosure statement

No potential conflict of interest was reported by the author(s).

Funding

The authors acknowledge FAPESP [grant numbers 2019/18388-1 and 2021/12959-7] for the grants of João Victor de Sousa Araujo and Rafael Emil Klumpp.

Data availability

The raw/processed data required to reproduce these findings cannot be shared at this time as the data also forms part of an ongoing study. However, part of the results is shared in the supplemental material.

ORCID

João Victor de Sousa Araujo http://orcid.org/0000-0001-6375-0480
Mariana Xavier Milagre http://orcid.org/0000-0003-2048-2863
Rafael Emil Klumpp http://orcid.org/0000-0003-3851-3277
Uyime Donatus http://orcid.org/0000-0001-8871-3571
Isolda Costa http://orcid.org/0000-0002-4987-3334

References

[1] Balbo A, Frignani A, Grassi V, et al. Corrosion inhibition by anionic surfactants of AA2198 Li-containing aluminium alloy in chloride solutions. Corros Sci. 2013;73:80–88. doi:10.1016/j.corsci.2013.03.027.

[2] Astarita A, Tucci F, Silvestri AT, et al. Dissimilar friction stir lap welding of AA2198 and AA7075 sheets: forces, microstructure and mechanical properties. Int J Adv Manuf Technol. 2021;117:1045–1059. doi:10.1007/s00170-021-07816-7.

[3] Warner T. Recently-developed aluminium solutions for aerospace applications. Mater Sci Forum. 2006;519–521:1271–1278. doi:10.4028/www.scientific.net/MSF.519-521.1271.

[4] Moreto JA, Gamboni OC, Marino CEB, et al. Corrosion behavior of Al and Al-Li alloys used as aircraft materials. Corros Prot Mater. 2012;31:60–64.

[5] Cavaliere P, Cabibbo M, Panella F, et al. 2198 Al–Li plates joined by friction stir welding: mechanical and microstructural behavior. Mater Des. 2009;30:3622–3631. doi:10.1016/j.matdes.2009.02.021.

[6] Garner A, Tromans D. Direct observation of intergranular corrosion in AI-4 Wt% Cu alloy. Corrosion. 1979;35:55–60. doi:10.5006/0010-9312-35.2.55.

[7] Chen Y, Pan X, Zhang C, et al. Influence of foreign object impact mode on fatigue performance of 2198-T8 Al-Li alloy thin sheets for fuselage. Fatigue Fract Eng Mater Struct. 2021;44:115–128. doi:10.1111/ffe.13338.

[8] Gloria A, Montanari R, Richetta M, et al. Alloys for aeronautic applications : state of the Art and perspectives. Metals. 2019;662:1–26. doi:10.3390/met9060662.

[9] Guan R, Lou H, Huang H, et al. Development of aluminum alloy materials: current status, trend, and prospects. Chinese J Eng Sci. 2020;22:68. doi:10.15302/J-SSCAE-2020.05.013.

[10] Wang W, Zhang L. Demand of China's aeronautics industry for Al-Li alloy. Nonferrous Met Proc (In Chinese). 2019;48:7–10.

[11] de Sousa Araujo JV, de F A, Bugarin S, et al. Thermomechanical treatment and corrosion resistance correlation in the AA2198 Al–Cu–Li alloy. Corros Eng Sci Technol. 2019;54:575–586. doi:10.1080/1478422X.2019.1637077.

[12] Buchheit RG. Local dissolution phenomena associated with S phase (Al_2CuMg) particles in aluminum Alloy 2024-T3. J Electrochem Soc. 1997;144:2621. doi:10.1149/1.1837874.

[13] Kowal K, DeLuccia J, Josefowicz JY, et al. In situ atomic force microscopy observations of the corrosion behavior of aluminum-copper alloys. J Electrochem Soc. 1996;143:2471–2481. doi:10.1149/1.1837033.

[14] Liao RPWCM, Olive JM, Gao M. In-situ monitoring of pitting corrosion in aluminium alloy 2024. Corrosion. 1998;54:451–458.

[15] Rao ACU, Vasu V, Govindaraju M, et al. Stress corrosion cracking behaviour of 7xxx aluminum alloys: A literature review. Trans Nonferrous Met Soc China (English Ed). 2016;26:1447–1471. doi:10.1016/S1003-6326(16)64220-6.

[16] de Sousa Araujo JV, Donatus U, Queiroz FM, et al. On the severe localized corrosion susceptibility of the AA2198-T851 alloy. Corros Sci. 2018;133:132–140. doi:10.1016/j.corsci.2018.01.028.

[17] de Souza Carvalho Machado C, Donatus U, Milagre MX, et al. Correlating the modes of corrosion with microstructure in the friction stir welded AA2198-T8 alloy in aqueous hydrogen peroxide-chloride medium. Corrosion. 2019;75:628–640. doi:10.5006/3054.

[18] Boag A, Hughes A, Glenn A. Corrosion of AA2024-T3 part I: localised corrosion of isolated IM particles. Corros Sci. 2011;53:17–26. doi:10.1016/j.corsci.2010.09.009.

[19] Glenn A, Muster T, Luo C, et al. Corrosion of AA2024-T3 Part III: propagation. Corros Sci. 2011;53:40–50. doi:10.1016/j.corsci.2010.09.035.

[20] Queiroz FM, Magnani M, Costa I, et al. Investigation of the corrosion behaviour of AA 2024-T3 in low concentrated chloride media. Corros Sci. 2008;50:2646–2657. doi:10.1016/j.corsci.2008.06.041.

[21] Birbilis N, Zhu YM, Kairy SK, et al. A closer look at constituent induced localised corrosion in Al-Cu-Mg alloys. Corros Sci. 2016;113:160–171. doi:10.1016/j.corsci.2016.10.018.

[22] Hughes A, Boag A, Glenn A. Corrosion of AA2024-T3 Part II: co-operative corrosion. Corros Sci. 2011;53:27–39. doi:10.1016/j.corsci.2010.09.030.

[23] Vukmirovic MB, Dimitrov N, Sieradzki K. Dealloying and corrosion of Al alloy 2024-T3. J Electrochem Soc. 2002;149:B428. doi:10.1149/1.1498258.

[24] Milagre MX, Donatus U, Machado CSC, et al. Comparison of the corrosion resistance of an Al–Cu alloy and an Al–Cu–Li alloy. Corros Eng Sci Technol. 2019;54:402–412. doi:10.1080/1478422X.2019.1605472.

[25] Blanc C, Lavelle B, Mankowski G. The role of precipitates enriched with copper on the susceptibility to pitting corrosion of the 2024 aluminium alloy. Corros Sci. 1997;39:495–510. doi:10.1016/S0010-938X(97)86099-4.

[26] Lacroix L, Ressier L, Blanc C, et al. Combination of AFM, SKPFM, and SIMS to study the corrosion behavior of S-phase particles in AA2024-T351. J Electrochem Soc. 2008;155:131–137. doi:10.1149/1.2833315.

[27] Larignon C, Alexis J, Andrieu E, et al. Combined Kelvin probe force microscopy and secondary ion mass spectrometry for hydrogen detection in corroded 2024 aluminium alloy. Electrochim Acta. 2013;110:484–490. doi:10.1016/j.electacta.2013.02.063.

[28] Queiroz FM, De Melo HG, Costa I. Effect of intermetallics on the corrosion of Al 2024-T3 alloy in solutions with different chloride concentration. Mater Sci Forum. 2008;587–588:415–419. doi:10.4028/www.scientific.net/msf.587-588.415.

[29] long Ma Y, rong Zhou X, min Meng X, et al. Influence of thermomechanical treatments on localized corrosion susceptibility and propagation mechanism of AA2099 Al–Li alloy. Trans Nonferrous Met Soc China. 2016;26:1472–1481. doi:10.1016/S1003-6326(16)64252-8.

[30] Moreto JA, Marino CEB, Bose Filho WW, et al. SVET, SKP and EIS study of the corrosion behaviour of high strength Al and Al-

Li alloys used in aircraft fabrication. Corros Sci. 2014;84:30–41. doi:10.1016/j.corsci.2014.03.001.

[31] Ma Y, Zhou X, Liao Y, et al. Localised corrosion in AA 2099-T83 aluminium-lithium alloy: the role of grain orientation. Corros Sci. 2016;107:41–48. doi:10.1016/j.corsci.2016.02.018.

[32] Luo C, Zhang X, Zhou X, et al. Characterization of localized corrosion in an Al-Cu-Li alloy. J Mater Eng Perform. 2016;25:1811–1819. doi:10.1007/s11665-016-2010-y.

[33] Ma Y, Zhou X, Huang W, et al. Localized corrosion in AA2099-T83 aluminum-lithium alloy: The role of intermetallic particles. Mater Chem Phys. 2015;161:201–210. doi:10.1016/j.matchemphys.2015.05.037.

[34] Zhang X, Zhou X, Ma Y, et al. The propagation of localized corrosion in Al-Cu-Li alloy. Surf Interface Anal. 2016;48:745–749. doi:10.1002/sia.5890.

[35] Zhou X, Luo C, Ma Y, et al. Grain-stored energy and the propagation of intergranular corrosion in AA2XXX aluminium alloys. Surf Interface Anal. 2013;45:1543–1547. doi:10.1002/sia.5218.

[36] Guérin M, Andrieu E, Odemer G, et al. Effect of varying conditions of exposure to an aggressive medium on the corrosion behavior of the 2050 Al – Cu – Li alloy. Corros Sci. 2014;85:455–470. doi:10.1016/j.corsci.2014.04.042.

[37] Buchheit RG, Moran JP, Stoner GE. Electrochemical behavior of the T1 (Al_2CuLi) intermetallic compound and its role in localized corrosion of Al-2%Li-3%Cu alloys. Corrosion. 1994;50:120–130. doi:10.5006/1.3293500.

[38] Li M, Seyeux A, Wiame F, et al. Insights on the Al-Cu-Fe-Mn intermetallic particles induced pitting corrosion of Al-Cu-Li alloy. Corros Sci. 2020;176:109040. doi:10.1016/j.corsci.2020.109040.

[39] Lei X, Saatchi A, Ghanbari E, et al. Studies on Pitting Corrosion of Al-Cu-Li alloys Part I: effect of Li addition by microstructural, electrochemical, In-situ, and Pit depth analysis. Materials. 2019;12:1600,. doi:10.3390/ma12101600.

[40] Zhu Y, Sun K, Garves J, et al. Micro- and nano-scale intermetallic phases in AA2070-T8 and their corrosion behavior. Electrochim Acta. 2019;319:634–648. doi:10.1016/j.electacta.2019.05.028.

[41] Zhu Y, Poplawsky JD, Li S, et al. Localized corrosion at nm-scale hardening precipitates in Al-Cu-Li alloys. Acta Mater. 2020;189:204–213. doi:10.1016/j.actamat.2020.03.006.

[42] de S. Araujo JV, da Silva RMP, Donatus U, et al. Microstructural, electrochemical and localized corrosion characterization of the AA2198-T851 alloy. Mater Res. 2020;23; doi:10.1590/1980-5373-mr-2020-0161.

[43] Sousa Araujo JV, Milagre MX, Ferreira RO, et al. Exfoliation and intergranular corrosion resistance of the 2198 Al–Cu–Li alloy with different thermomechanical treatments. Mater Corros. 2020;71:1957–1970. doi:10.1002/maco.202011839.

[44] Xu X, Hao M, Chen J, et al. Role of intermetallic phases in initiation and propagation of intergranular corrosion of an AlLiCuMg alloy. Mater Sci. 2021: 1–43. doi:10.48550/arXiv.2106.15160.

[45] Li M, Seyeux A, Wiame F, et al. Localized corrosion induced surface modifications of Al-Cu-Li alloy studied by ToF-SIMS 3D imaging. Mater Degrad. 2021;5:23. doi:10.1038/s41529-021-00170-9.

[46] Xu X, Hao M, Chen J, et al. Role of constituent intermetallic phases and precipitates in initiation and propagation of intergranular corrosion of an Al-Li-Cu-Mg alloy. Corros. Sci. 2022;201:110294. doi:10.1016/j.corsci.2022.110294.

[47] Zhang X, Lv Y, Zhou X, et al. Corrosion behaviour of 2A97-T8 Al-Cu-Li alloy extrusion. J Alloys Compd. 2021;162872; doi:10.1016/j.jallcom.2021.162872.

[48] Glenn AM, Hughes AE, MacRae CM, et al. Observations on the early stages of corrosion on AA2099-T83. Microsc Microanal. 2020;6:1–16. doi:10.1017/s1431927620001634.

[49] Kosari A, Tichelaar F, Visser P, et al. Dealloying-driven local corrosion by intermetallic constituent particles and dispersoids in aerospace aluminium alloys. Corros Sci. 2020;177:108947. doi:10.1016/j.corsci.2020.108947.

[50] Ji Y, Xu Y, Zhang B, et al. Review of micro-scale and atomic-scale corrosion mechanisms of second phases in aluminum alloys. Trans Nonferrous Met Soc China. 2021;31:3205–3227. doi:10.1016/S1003-6326(21)65727-8.

[51] Liew Y, Örnek C, Pan J, et al. Towards understanding micro-galvanic activities in localised corrosion of AA2099 aluminium alloy. Electrochim Acta. 2021;392:139005. doi:10.1016/j.electacta.2021.139005.

[52] Ghanbari E, Saatchi A, Lei X, et al. Studies on Pitting Corrosion of Al-Cu-Li Alloys Part II: breakdown potential and Pit initiation. Materials. 2019;12:1786. doi:10.3390/ma12111786.

[53] Zhu Y, Sun K, Frankel GS. Intermetallic phases in Aluminum Alloys and their roles in localized corrosion. J Electrochem Soc. 2018;165:C807–C820. doi:10.1149/2.0931811jes.

[54] Ghanbari E, Saatchi A, Lei X, et al. Studies on pitting corrosion of Al–Cu–Li alloys Part III: passivation kinetics of AA2098–T851 Based on the point defect model. Materials. 2019;12:1912. doi:10.3390/ma12121912.

[55] Carangelo A, Curioni M, Acquesta A, et al. Application of EIS to in situ characterization of hydrothermal sealing of anodized aluminum alloys: comparison between hexavalent chromium-based sealing, hot water sealing and cerium-based sealing. J Electrochem Soc. 2016;163:C619–C626. doi:10.1149/2.0231610jes.

[56] Ding Z, Smith BA, Hebert RR, et al. Morphology perspective on chromic acid anodizing replacement by thin film sulfuric acid anodizing. Surf Coatings Technol. 2018;350:31–39. doi:10.1016/j.surfcoat.2018.07.008.

[57] Harscoet E, Froelich D. Use of LCA to evaluate the environmental benefits of substituting chromic acid anodizing (CAA). J Clean Prod. 2008;16:1294–1305. doi:10.1016/j.jclepro.2007.06.010.

[58] Yu X, Cao C. Electrochemical study of the corrosion behavior of Ce sealing of anodized 2024 aluminum alloy. Thin Solid Films. 2003;423:252–256. doi:10.1016/S0040-6090(02)01038-6.

[59] García-Rubio M, Ocón P, Climent-Font A, et al. Influence of molybdate species on the tartaric acid/sulphuric acid anodic films grown on AA2024 T3 aerospace alloy. Corros Sci. 2009;51:2034–2042. doi:10.1016/j.corsci.2009.05.034.

[60] Marzocchi V, Iglesias-Rubianes L, Thompson GE, et al. The influence of tartaric acid additions on the anodizing behaviour of AA2024-T3 alloy in sulphuric acid. Corros Rev. 2007;25; doi:10.1515/CORRREV.2007.25.3-4.461.

[61] Wang LSR, Wang L, He C, et al. Studies on the sealing processes of corrosion resistant coatings formed on 2024 aluminium alloy with tartaric-sulfuric anodizing. Surf Coat Technol. 2007;360:369–375.

[62] Zahavi J, Kerbel H, Korotkina O. A-C anodizing processes of Aluminum alloys. J Electrochem Soc. 1982;129:1572–1579. doi:10.1149/1.2124211.

[63] Iglesias-Rubianes L, Garcia-Vergara SJ, Skeldon P, et al. Cyclic oxidation processes during anodizing of Al-Cu alloys. Electrochim Acta. 2007;52:7148–7157. doi:10.1016/j.electacta.2007.05.052.

[64] Curioni M, Saenz De Miera M, Skeldon P, et al. Macroscopic and local filming behavior of AA2024 T3 aluminum alloy during anodizing in sulfuric acid electrolyte. J Electrochem Soc. 2008;155:387–395. doi:10.1149/1.2931522.

[65] Saenz de Miera M, Curioni M, Skeldon P, et al. Modelling the anodizing behaviour of aluminium alloys in sulphuric acid through alloy analogues. Corros Sci. 2008;50:3410–3415. doi:10.1016/j.corsci.2008.09.019.

[66] Saenz de Miera M, Curioni M, Skeldon P, et al. The behaviour of second phase particles during anodizing of aluminium alloys. Corros Sci. 2010;52:2489–2497. doi:10.1016/j.corsci.2010.03.029.

[67] Nickel D, Dietrich D, Morgenstern R, et al. Anodisation of aluminium alloys by micro-capillary technique as a tool for reliable, cost-efficient, and quick process parameter determination. Adv Mater Sci Eng. 2016;2016:1–12. doi:10.1155/2016/1374897.

[68] Fares ABC, Belouchrani MA, Bellayer S, et al. Influence of intermetallic compounds and metallurgical state of the 2017A aluminium alloy on the morphology of alumina films developed by anodic oxidation. J Tribol Surf Eng. 2011;2:239–251.

[69] Fares C, Boudiaf A, Belouchrani MEA, et al. Microstructural characterisation of oxide layer developed by sulphuric

anodisation on 2017A alloys. Int J Mater Res. 2013;104:1108–1113. doi:10.3139/146.110962.

[70] Bononi M, Giovanardi R. Hard anodizing of AA2011-T3 Al-Cu-Pb-Bi free-cutting alloy: improvement of the process parameters. Corros Sci. 2018;141:63–71. doi:10.1016/j.corsci.2018.07.004.

[71] Abdel-Gawad SA, Osman WM, Fekry AM. Characterization and corrosion behavior of anodized aluminum alloys for military industries applications in artificial seawater. Surf Interf. 2019;14:314–323. doi:10.1016/j.surfin.2018.08.001.

[72] Veys-Renaux D, Chahboun N, Rocca E. Anodizing of multiphase aluminium alloys in sulfuric acid: in-situ electrochemical behaviour and oxide properties. Electrochim Acta. 2016;211:1056–1065. doi:10.1016/j.electacta.2016.06.131.

[73] Elkilany HA, Shoeib MA, Abdel-Salam OE. Influence of hard anodizing on the mechanical and corrosion properties of different aluminum alloys. Metallogr Microstruct Anal. 2019;8:861–870. doi:10.1007/s13632-019-00594-5.

[74] Viejo F, Coy AE, García-García FJ, et al. Enhanced performance of the AA2050-T8 aluminium alloy following excimer laser surface melting and anodising processes. Thin Solid Films. 2010;518:2722–2731. doi:10.1016/j.tsf.2009.09.121.

[75] Ma Y, Zhou X, Thompson GE, et al. Discontinuities in the porous anodic film formed on AA2099-T8 aluminium alloy. Corros Sci. 2011;53:4141–4151. doi:10.1016/j.corsci.2011.08.023.

[76] Ma Y, Zhou X, Thompson GE, et al. Anodic film formation on AA 2099-T8 Aluminum Alloy in tartaric–sulfuric acid. J Electrochem Soc. 2011;158:C17–C22. doi:10.1149/1.3523262.

[77] Ma Y, Chen X, Zhou X, et al. Microstructural origin of localized corrosion in anodized AA2099-T8 aluminium–lithium alloy. Surf Interface Anal. 2016;48:739–744. doi:10.1002/sia.5856.

[78] Ma Y, Zhou X, Li K, et al. Corrosion and anodizing behavior of T1 (Al_2CuLi) precipitates in Al-Cu-Li alloy. J Electrochem Soc. 2019;166:C296–C303. doi:10.1149/2.0891912jes.

[79] Bononi M, Conte M, Giovanardi R, et al. Hard anodizing of AA2099-T8 aluminum–lithium–copper alloy: Influence of electric cycle, electrolytic bath composition and temperature. Surf Coatings Technol. 2017;325:627–635. doi:10.1016/j.surfcoat.2017.07.028.

[80] Wu H, Ma Y, Huang W, et al. Effect of iron-containing intermetallic particles on film structure and corrosion resistance of anodized AA2099 alloy. J Electrochem Soc. 2018;165:C573–C581. doi:10.1149/2.1361809jes.

[81] Liu J, Rong G, Cen S, et al. Dissolution behavior of intermetallic particles in AA2297-T87 during anodizing in adipic-sulfuric acid. J Electrochem Soc. 2018;165:C980–C990. doi:10.1149/2.0061816jes.

[82] Ma Y, Wu H, Zhou X, et al. Corrosion behavior of anodized Al-Cu-Li alloy: The role of intermetallic particle-introduced film defects. Corros Sci. 2019;158; doi:10.1016/j.corsci.2019.108110.

[83] Samaniego-Gámez PO, Almeraya-Calderon F, Maldonado-Bandala E, et al. Corrosion behavior of AA2055 aluminum-lithium alloys anodized in the presence of sulfuric acid solution. Coatings. 2021;11:1278. doi:10.3390/coatings11111278.

[84] Dorin T, Vahid A, Lamb J. Aluminium lithium alloys. In: Roger N. Lumley , editor. Fundamentals of aluminium metallurgy. Melbourne: Elsevie; 2018. p. 387–438. doi:10.1016/B978-0-08-102063-0.00011-4.

[85] Han B, Chen Y, Tao W, et al. Microstructural evolution and interfacial crack corrosion behavior of double-sided laser beam welded 2060/2099 Al-Li alloys T-joints. Mater Des. 2017;135:353–365. doi:10.1016/j.matdes.2017.09.042.

[86] Gao C, Ma Y, Tang L, et al. Microstructural evolution and mechanical behavior of friction spot welded 2198-T8 Al-Li alloy during aging treatment. Mater Des. 2017;115:224–230. doi:10.1016/j.matdes.2016.11.045.

[87] Zhu P, Ma Y, Li K, et al. Sealing of anodized AA2099-T83 Al-Cu-Li alloy with layered double hydroxides for high corrosion resistance at reduced anodic film thickness. Surf Coatings Technol. 2020;394:125852. doi:10.1016/j.surfcoat.2020.125852.

[88] de Souza Carvalho Machado C, Donatus U, Milagre MX, et al. How microstructure affects localized corrosion resistance of stir zone of the AA2198-T8 alloy after friction stir welding. Mater Charact. 2021;174:111025. doi:10.1016/j.matchar.2021.111025.

[89] Donatus U, Ferreira RO, Mogili NVV, et al. Corrosion and anodizing behaviour of friction stir weldment of AA2198-T851 Al-Cu-Li alloy. Mater Chem Phys. 2018;219:493–511. doi:10.1016/j.matchemphys.2018.08.053.

[90] Donatus U, Terada M, Ospina CR, et al. On the AA2198-T851 alloy microstructure and its correlation with localized corrosion behaviour. Corros Sci. 2018;131:300–309. doi:10.1016/j.corsci.2017.12.001.

[91] Klumpp RE, Donatus U, da Silva RMP, et al. Corrosion protection of the AA2198-T8 alloy by environmentally friendly organic-inorganic sol-gel coating based on bis-1,2-(triethoxysilyl) ethane. Surf Interface Anal. 2020: 1–16. doi:10.1002/sia.6919.

[92] Donatus U, Berbel LO, Costa I. Qualitative use of potentiodynamic polarization and anodic hydrogen evolution in the assessment of corrosion susceptibility in AA2198-T851 Al–Cu–Li alloy. Mater Corros. 2018;69:1375–1388. doi:10.1002/maco.201810108.

[93] Balbo A, Frignani A, Grassi V, et al. Electrochemical behaviour of AA2198 and AA2139 in neutral solutions. Mater Corros. 2015;66:796–802. doi:10.1002/maco.201408059.

[94] Alexopoulos ND, Proiou A, Examilioti T, et al. Effect of artificial aging on the mechanical performance of (Al-Cu) 2024 and (Al-Cu-Li) 2198 aluminum alloys. Procedia Struct Integr. 2016;2:3782–3783. doi:10.1016/j.prostr.2016.06.470.

[95] Alexopoulos ND, Proiou A, Dietzel W, et al. Mechanical properties degradation of (Al-Cu-Li) 2198 alloy due to corrosion exposure. Procedia Struct Integr. 2016;2:597–603. doi:10.1016/j.prostr.2016.06.077.

[96] Alexopoulos ND, Migklis E, Stylianos A, et al. Fatigue behavior of the aeronautical Al–Li (2198) aluminum alloy under constant amplitude loading. Int J Fatigue. 2013;56:95–105. doi:10.1016/j.ijfatigue.2013.07.009.

[97] Charalampidou C, Dietzel W, Zheludkevich M, et al. Corrosion-induced mechanical properties degradation of Al-Cu-Li (2198-T351) aluminium alloy and the role of side-surface cracks. Corros Sci. 2021;183:109330. doi:10.1016/j.corsci.2021.109330.

[98] Georgoulis D, Charalampidou CM, Siskou N, et al. Corrosion behaviour of AA2198–T8 and AA2024-T3 alloy in 3.5% aqueous solution. Procedia Struct Integr. 2020;28:2297–2303. doi:10.1016/j.prostr.2020.11.076.

[99] Carrick DM, Hogg SC, Wilcox GD. Corrosion of an advanced Al-Cu-Li alloy for aerospace applications. Mater Sci Forum. 2013;765:629–633. doi:10.4028/www.scientific.net/MSF.765.629.

[100] Donatus U, Oluwatosin Bodunrin M, Olayinka A, et al. Corrosion resistance of precipitation-hardened Al alloys: a comparison between new generation Al-Cu-Li and conventional alloy. In: Aluminium alloys. IntechOpen. 2020. doi:10.5772/intechopen.92807.

[101] Alenia Aeronautica SPA, Alenia Aeronautica SPA. Anodizing process, with low environmental impact, for a workpiece of aluminium or aluminium alloys. European Patent Application EP. n.d.: 1233084 A2.

[102] Fratila-Apachitei L, Terryn H, Skeldon P, et al. Influence of substrate microstructure on the growth of anodic oxide layers. Electrochim Acta. 2004;49:1127–1140. doi:10.1016/j.electacta.2003.10.024.

[103] Moon S-M, Sakairi M, Takahashi H. Application of CSLM to the surface morphological study of Al 5052 alloy anodized in sulfuric acid solution. J Electrochem Soc. 2003;150:B473. doi:10.1149/1.1603248.

[104] Moon SM, Sakairi M, Takahashi H. Behavior of second-phase particles in Al5052 alloy during anodizing in a sulfuric acid solution CSLM observation. J Electrochem Soc. 2004;151:399–405. doi:10.1149/1.1752933.

[105] Parkhutik VP, Shershulsky VI. Theoretical modelling of porous oxide growth on aluminium. J Phys D Appl Phys. 1992;25:1258–1263. doi:10.1088/0022-3727/25/8/017.

[106] Lee W, Park SJ. Porous anodic aluminum oxide: anodization and templated synthesis of functional nanostructures. Chem Rev. 2014;114:7487–7556. doi:10.1021/cr500002z.

[107] Zhou X, Thompson GE, Skeldon P, et al. Film formation and detachment during anodizing of Al-Mg alloys. Corros Sci. 1999;41:1599–1613. doi:10.1016/S0010-938X(99)00007-4.

[108] Aksenov AA, Eskin DG, Belov NA. Multicomponent phase diagrams. Elsevier; 2005. doi:10.1016/B978-0-08-044537-3.X5000-8.

[109] Birbilis N, Buchheit RG. Electrochemical characteristics of intermetallic phases in Aluminum alloys. J Electrochem Soc. 2005;152:B140. doi:10.1149/1.1869984.

[110] Buchheil RG. A compilation of corrosion potentials reported for intermetallic phases in aluminum alloys. J Electrochem Soc. 1995;142:3994–3996. doi:10.1149/1.2048447.

[111] de Sousa Araujo JV, Milagre MX, Ferreira RO, et al. Microstructural characteristics of the Al alloys: The dissimilarities among the 2XXX alloys series used in aircraft structures. Metallogr Microstruct Anal. 2020, doi:10.1007/s13632-020-00688-5.

[112] Ma Y, Zhou X, Thompson GE, et al. Distribution of intermetallics in an AA 2099-T8 aluminium alloy extrusion. Mater Chem Phys. 2011;126:46–53. doi:10.1016/j.matchemphys.2010.12.014.

[113] Liu Y, Arenas MA, Skeldon P, et al. Anodic behaviour of a model second phase: Al-20at.%Mg-20at.%Cu. Corros Sci. 2006;48:1225–1248. doi:10.1016/j.corsci.2005.05.007.

[114] de Miera MS. Effects of microstructure on anodizing of high strength aluminium alloys. Manchester: Manchester University; 2008.

[115] Sepulveda Y, Paez MA, Zagal JH, et al. Anodizing of al 2024-T3 in mixtures of sulphuric-boric acids. Boletín La Soc Chil Química. 2001;46; doi:10.4067/S0366-16442001000400003.

[116] Moutarlier V, Gigandet MP, Pagetti J, et al. Molybdate/sulfuric acid anodising of 2024-aluminium alloy: Influence of inhibitor concentration on film growth and on corrosion resistance. Surf Coatings Technol. 2003;173:87–95. doi:10.1016/S0257-8972(03)00511-5.

[117] MacRae CM, Hughes AE, Laird JS, et al. An examination of the composition and microstructure of coarse intermetallic particles in AA2099-T8, including Li detection. Microsc Microanal. 2018: 1–17. doi:10.1017/S1431927618000454.

[118] Saenz De Miera M, Curioni M, Skeldon P, et al. Preferential anodic oxidation of second-phase constituents during anodising of AA2024-T3 and AA7075-T6 alloys. Surf Interface Anal. 2010;42:241–246. doi:10.1002/sia.3191.